MECHANICAL BEHAVIOR OF RECYCLED ASPHALT MATERIAL UNDER DYNAMIC LOADING CONDITIONS

Martin H. Sadd, Arun Shukla
Arjun Tekalur and Qingli Dai
University of Rhode Island

March 2005

URITC PROJECT NO. 536186

PREPARED FOR

UNIVERSITY OF RHODE ISLAND
TRANSPORTATION CENTER

1. Report No	2. Government Accession No.	3. Recipient's Catalog No.
URITC 02-12	N/A	N/A

4. Title and Subtitle	5. Report Date
Mechanical Behavior of Recycled Asphalt Material Under Dynamic Loading Conditions	March 2005
	6. Performing Organization Code: N/A

7. Authors(s)	8. Performing Organization Report No.
Martin H. Sadd, Arun Shukla, Arjun Tekalur and Qingli Dai	

9. Performing Organization Name and Address	10. Work Unit No. (TRAIS)
	N/A
University of Rhode Island Mechanical Engineering & Applied Mechanics Department 92 Upper College Road Kingston, RI 02881	11. Contract or Grant No. URITC 536186
	13. Type of Report and Period Covered Final

12. Sponsoring Agency Name and Address	14. Sponsoring Agency Code
University of Rhode Island Transportation Research Center Carlotti Admin. Building, 75 Lower College Road Kingston, RI 02881	

15. Supplementary Notes

N/A

16. Abstract

This report describes activities and findings of a research project dealing with particular micromechanical behaviors of asphalt materials under time dependent loading conditions. The project involved both experimental studies and theoretical/numerical modeling. Experimental work included laboratory testing of compression, indirect tension and three-point bending fracture specimens with 30% reclaimed material (RAP). Testing included both quasi-static and dynamic loadings applied in a split Hopkinson pressure bar apparatus. Results of the experimental studies indicated significant differences in the failure mechanisms of all three types of samples. Much more aggregate failure was observed in samples subjected to dynamic loading conditions. Numerical modeling continued along methods established from our previous studies. This work employed finite element techniques to develop a microstructural model of heterogeneous asphalt materials. The model simulates the load transfer between aggregates and incorporates a damage mechanics approach to simulate the inelastic failure mechanisms in the binder material. The current numerical work has extended our modeling to rate dependent viscoelastic behavior using Schapery's non-linear viscoelastic damage coupled methods. These methods were numerically implemented using the user material subroutines within the ABAQUS commercial FEA code. Model results for several loading histories were in qualitative agreement with expected behavior and for a uniaxial test case, model results compared favorably with some particular experimental data.

17. Key Words	18. Distribution Statement
Recycled Asphalt, Dynamic Behavior, Finite Element Modeling, Asphalt Microstructure, Numerical Simulation	No restrictions. This document is available to the public through the University of Rhode Island Transportation Center, 75 Lower College Rd., Kingston, RI 02881

19. Security Classif. (of this report)	20. Security Classif. (of this page)	21. No. of Pages	22. Price
Unclassified	Unclassified	81	N/A

Form DOT F 1700.7 (8-72) Reproduction of completed page authorized (art. 5/94)

TABLE OF CONTENTS

List of Tables

List of Figures

1. INTRODUCTION

This report describes the research activity of a project investigating the micromechanical behavior of asphalt concrete. The project has been involved with both experimental studies and theoretical/numerical modeling efforts to better understand the mechanical compressive, tensile and fracture response of bituminous mixes. The overall program has been concerned with both the static and time-dependent/dynamic behaviors, and we have also included some studies directed at reclaimed asphalt product (RAP).

The experimental program has investigated compression, indirect tension and fracture testing of specimens under quasi-static and high strain rate loading regimes. Samples were made from materials donated by a local asphalt distributor, Cardi Corporation of Rhode Island, and the material included 30% RAP content. Compression and indirect tension testing used standard ASTM geometries and procedures, and the fracture studies used single edge notched, three-point bend beam specimens. Quasi-static loading was conducted in an Instron testing machine, while dynamic loading was done in a Split Hopkinson Pressure Bar apparatus.

Numerical modeling followed along methods established from our previous studies. This work employed finite element techniques to develop a microstructural model of heterogeneous asphalt materials. The model simulates the load transfer between aggregates and incorporates a damage mechanics approach to simulate the inelastic failure mechanisms in the binder material. The current numerical work has extended our modeling to rate dependent viscoelastic behavior using Schapery's non-linear viscoelastic damage coupled methods. These techniques were numerically implemented using the user material subroutines within the ABAQUS commercial FEA code.

Following this introduction, the report briefly describes some details on the mix design in Section 2. This is followed in Section 3 by a review of the quasi-static characterization under uniaxial compression and indirect tension. Section 4 describes the dynamic characterization studies, including some details on the Split Hopkinson Pressure Bar (SHPB) loading apparatus. Fracture studies are then presented in Section 5, giving some details on the static and dynamic fracture toughness results. Numerical modeling activities are discussed in Section 6, and the current work has been focused on the development of a damaged coupled viscoelastic time-depend model. As outlined in Section 8, portions of this work have been presented at several conferences and will soon appear in appropriate journals.

2. MIX DESIGN

Sample material preparation first involved deciding on the appropriate mix design. Asphalt is a complex heterogeneous material containing aggregate, binder/cement, additives and void space. Properties of such a material strongly depend on the ratio of these constituents and are commonly determined by standard ASTM testing. An additional factor related to our study was the planned inclusion of a particular percentage of reclaimed asphalt pavement (RAP) in the sample mix recipe. Following a locally accepted limit, we decided to use 30% RAP content in our sample material.

Asphalt samples for all testing programs were prepared using Marshall mix design procedures. Virgin asphalt used performance grade 64-22. Basic materials were obtained from Cardi Corporation of Rhode Island including: stone stockpiles of 3/4", 1/2" and 3/8"; and sand and RAP 3/4" and 3/8". Unfortunately, details of the RAP related to location, source, asphalt content, etc were not available. After collecting the raw materials, they were washed and dried in an oven, sampled and prepared for sieve analysis to obtain aggregate size percentages. The sieve analysis data are shown in Figs 2.1, 2.2 and 2.3 and are used for mix design procedures.

Marshall's mix design procedures were used for determining the optimum binder content (OBC) to be used in the mix. The gradation chart of the mix used in the study is shown in Fig 2.4. It may be noted that the aggregate gradation also meets the Superpave specification. In determining the design asphalt content for a particular blend or gradation of aggregates by the Marshall method, a series of test specimens is prepared for a range of different asphalt contents so that the test data curves show well-defined relationships. Tests are planned on the basis of ½ percent increments of asphalt content. To provide adequate data, at least three test specimens are prepared for each asphalt content selected. Each sample weighed approximately 1200g.

The Marshall testing machine is a compression-testing device designed to apply loads to test specimens through cylindrical segment testing heads (inside radius of curvature of 51 mm) at a constant crosshead displacement of 51 mm/min (2 in/min). Two perpendicular guideposts are included to allow the two segments to maintain horizontal positioning and free vertical movement during the test. It is equipped with a calibrated proving ring for determining the applied testing load and a flow meter for determining the amount of strain at the maximum load in the test. A universal testing machine equipped with the suitable load and deformation indicating devices may be used instead of the Marshall testing frame.

The bulk specific gravity test was performed as soon as the freshly compacted specimens had cooled to room temperature. This test was performed according to ASTM D 2726, *Bulk Specific Gravity Of Compacted Bituminous Mixtures Using Saturated Surface Dry Specimens* as described below:

(a) The average bulk specific gravity value for each asphalt content value is obtained.

(b) The average unit weight for each asphalt content is determined by multiplying the average bulk specific gravity value by the density of water (1000 kg/m^3).

(c) The theoretical maximum specific gravity (ASTM D 2041) is determined for at least two asphalt contents, preferably on mixes at or near the design asphalt content. An average value for the effective specific gravity of the total aggregate is then calculated from these values.

(d) Using the effective and bulk specific gravity of the total aggregate, the average bulk specific gravities of the compacted mix, the specific gravity of the asphalt, and the maximum specific gravity of the mix determined in (c), the percent asphalt absorbed by weight of dry aggregate, percent air voids (V_a), percent voids filled with asphalt (VFA) and percent voids in mineral aggregate (VMA) are calculated. These are used in design procedure.

The Marshall's stability and flow test was performed as per ASTM standard D1559 on an Instron universal testing machine. Fig. 2.5 illustrates stability vs. asphalt content; Fig. 2.6 plots percent air voids (V_a) vs. asphalt content; and Fig. 2.7 shows flow vs. asphalt content. These results were used to determine the appropriate asphalt content of the mix. The OBC selected was 5.4%.

Specimens for the individual tests were prepared as described below:

Static Indirect Tension Test:

The specimen prepared for Marshall's test was a 4-inch diameter and 2.5-inch height cylinder. This size and shape sample is appropriate for the indirect tension test.

Static Compression Test:

The specimen dimension required for this test is 4-inch diameter and 4-inch height cylinder. Special molds, which are capable of making such specimens, were designed and machined in our shop. The specimens were prepared by manual compaction using the Marshall method. Three different levels of compaction were used, namely 60, 80 and 90 blows on each end. The desired

compaction was obtained by testing the compacted specimens for bulk specific gravity. The obtained values were used for matching with the standard Marshall's specimens. The best matching level was used for testing.

Static Fracture Toughness Test:

The specimen required for this test is a rectangular beam with a length to width ratio of 4. The specimens are prepared by compacting hot mix aggregates and asphalt in a specially designed and manufactured mold. The level of compaction is found by trial and error and experimental verification of the properties of the beam as compared to the standard Marshall's specimen.

Dynamic Indirect Test:

The size of specimen used for this test is 4-inch diameter and 2-inch high cylinder. The specimens were prepared by the standard Marshall method and cut to required height on a diamond tipped cutter.

Dynamic Compression Test:

The specimen dimensions required for the dynamic compression test is a cylinder of diameter 1.75 inch and height ½ inch. Such specimens were cored from the standard Marshall specimen using a core bit on a universal drilling machine.

Dynamic Fracture Toughness Test:

The specimen dimensions and preparation were the same as used in the static fracture toughness tests.

The cutting and coring operations used to prepare samples for the dynamic testing were carefully done to minimize any heat build up or aggregate damage.

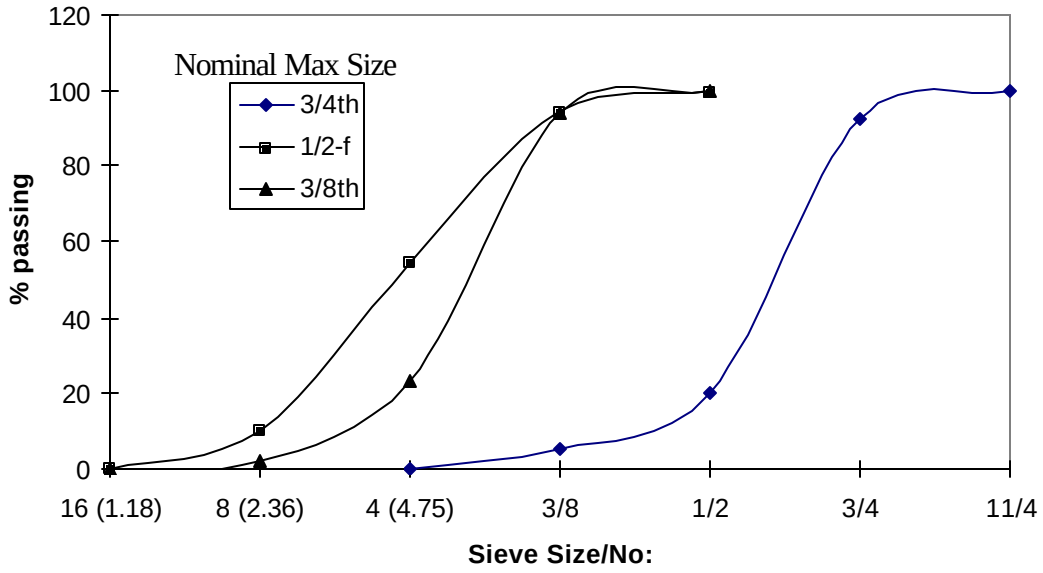

Fig. 2.1 Gradation of coarse aggregates

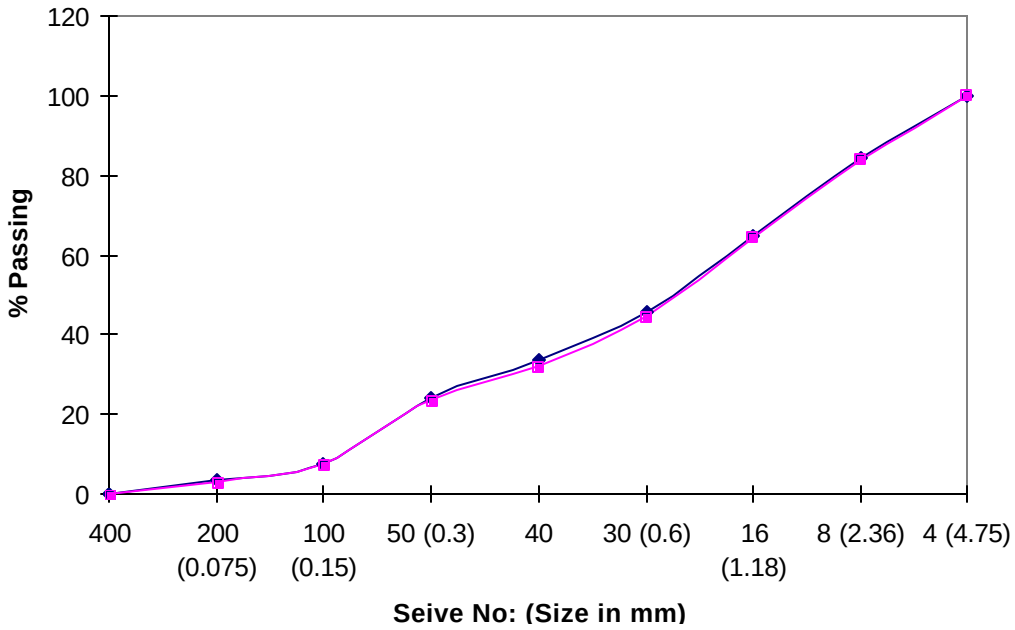

Fig. 2.2 Sieve analysis for sand

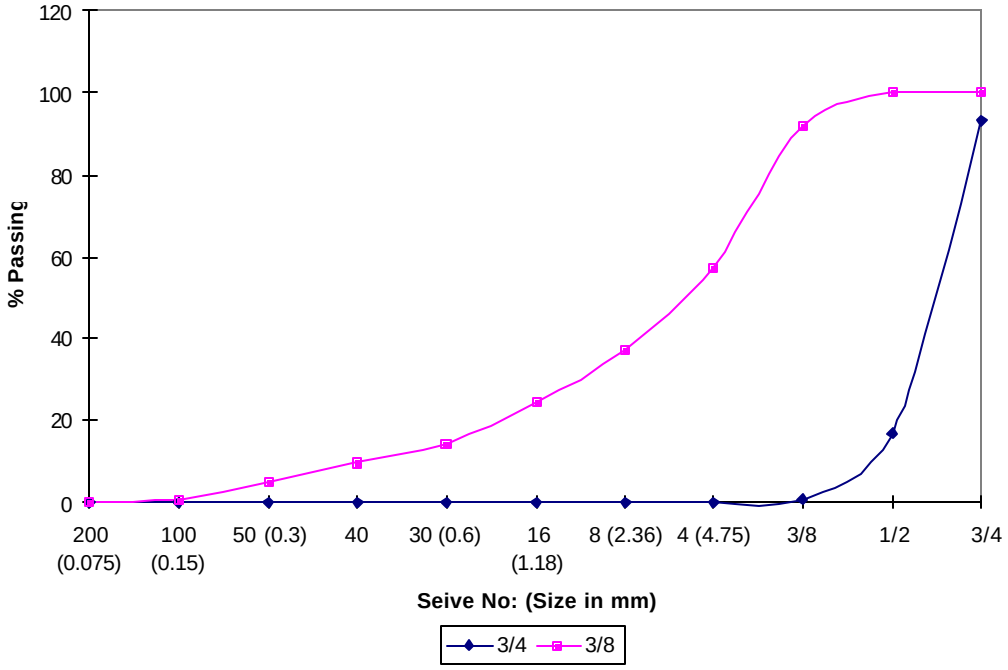

Fig. 2.3 Gradation of RAP

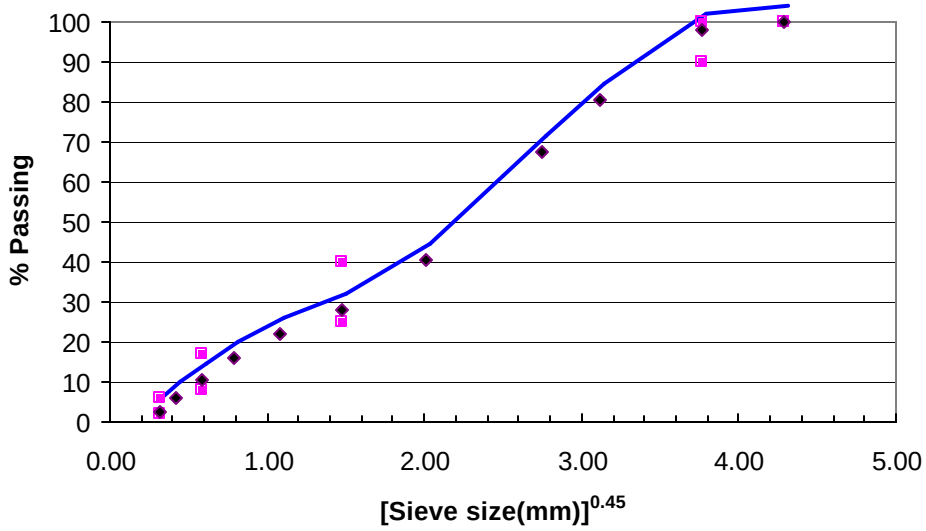

Fig. 2.4 Gradation chart of the mix containing 30% RAP

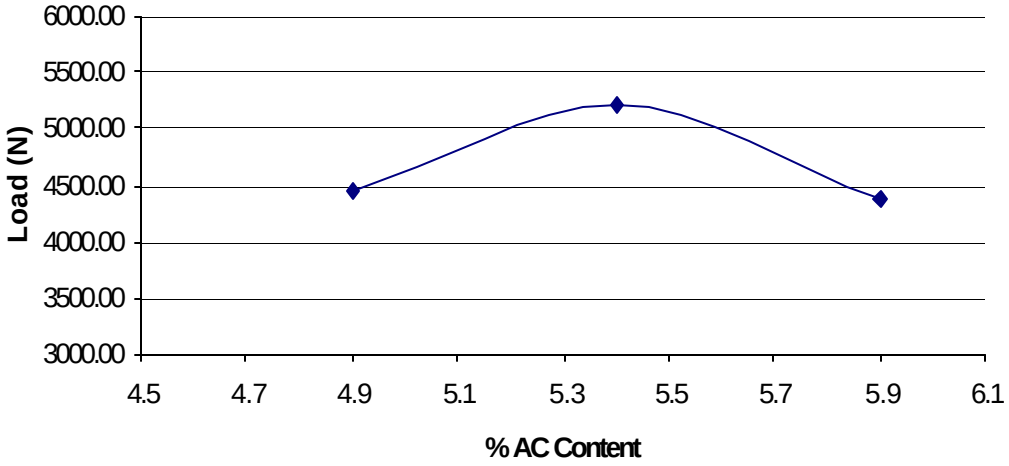

Fig. 2.5 Marshall stability vs. asphalt content

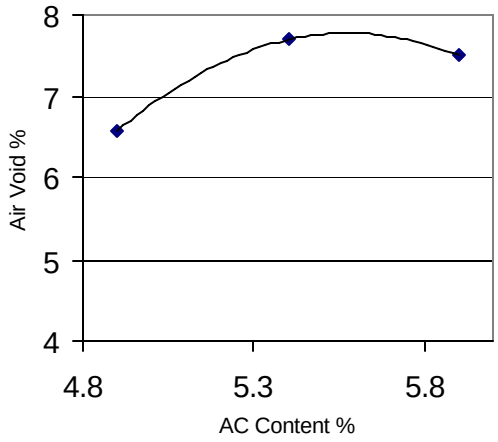

Fig. 2.6 VTM (air voids) vs. asphalt content

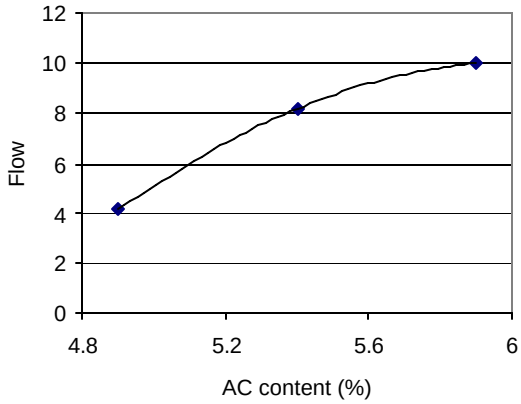

Fig. 2.7 Marshall flow vs. asphalt content

3. QUASI - STATIC CHARACTERIZATION

Quasi-static loading is a process in which the sample is loaded so slowly that the system remains close to equilibrium at all times. The loading time-scale should then be much longer than the relaxation time of the system, and all inertia effects should remain vanishingly small. In applied mechanics, this situation is also termed as low strain rate testing.

3.1 Quasi-Static Compression Behavior

The standard cylindrical specimen was adopted for this study as prescribed in ASTM standard D1074. The specimen blank shown in Fig. 3.1 had a diameter of 101.6 mm and a height of 101.6mm. Compression testing was done on Instron 5585 Universal Testing Machine. The crosshead movement of 51 mm/min (2 in/min) was maintained. To avoid friction between the sample and the crosshead, a thin layer of talc was applied. During sample preparation, the number of blows given to each side of the specimen was varied. Three different levels of compaction were tried, namely, 60, 80 and 90 blows. The compacted specimens were then tested for bulk specific gravity. The bulk specific gravity of a standard Marshall specimen was compared to these trial results and it was found that 80 blows matched the best with the standard specimen. The setup for the compression testing is shown in Fig. 3.2. It was ensured that the loading platens of the crosshead were completely touching the specimen top before balancing the load cell and extensometer. Three samples were tested for static compressive behavior.

Results obtained from the quasi-static compression tests are shown in Figs. 3.3-3.5. Fig. 3.3 plots the quasi-static compressive stress strain behavior for specimen compacted using 60 blows on each end. In the initial region of the graph, there exists small instability and the response smoothens out as the test proceeds. A peak stress value of 3.72 MPa was obtained for this specimen at a corresponding strain of approximately 0.03. Fig. 3.4 plots the quasi-static compressive stress strain behavior for specimen compacted using 80 blows on each end. As evident from the figure, the slope of all the tests was almost equal and an average peak stress of 3.55 MPa was obtained at a corresponding strain of approximately 0.015. A composite plot comprising the quasi-static stress strain behavior of all the specimens with different levels of compaction is shown in Fig. 3.5.

3.2 Quasi-Static Tension Behavior

Tensile properties of brittle materials are often difficult to determine when using standard “dog bone” specimens due to the inherent difficulties in applying the loadings. To overcome these difficulties, the indirect tension (splitting) test geometry has been developed, and is now

widely used for concrete materials. The geometry is shown in Fig. 3.6, and the peak compressive load obtained from the test can be used to calculate the tensile properties of the material. From theory of elasticity, a circular disk under concentrated diametrical compressive loading develops tensile stresses on the center plane ($x = 0$) given by

$$\sigma_x = \frac{2P}{\pi LD}\ ,\ \sigma_y = \frac{2P}{\pi LD}\left[\frac{D^2}{y(D-y)} - 1\right] \tag{3.1}$$

where P = applied load, L = sample thickness and D = sample diameter. The uniform stress σ_x relation provides a relationship to determine the failure stress (tensile strength) in terms of measured values of sample geometry and load.

A special fixture was designed and fabricated to hold the specimen in place and to measure the horizontal displacement when the load is applied vertically. The setup is shown in Fig. 3.7. As shown, two loading strips are used to avoid stress concentration and to obtain loading along a line perpendicular to the sample face.

Five samples were tested for static tension behavior. Results obtained from these individual tests, along with average, standard deviation and 95% confidence are provided in Table 3.1. A typical load-extension curve obtained from the testing is shown in Fig. 3.8. The peak loads obtained from the load-extension curves were used in calculating the splitting stress suing relation (3.1). The average splitting strength was found to be 1.32 ± 0.04 MPa.

Table 3.1 Experimental Results Obtained from Quasi-Static Indirect Tension Tests

Test No.	***Peak Load (kN)***	***Splitting Stress (MPa)***
1	13.14	1.30
2	12.70	1.25
3	13.74	1.36
4	14.02	1.38
5	13.25	1.31
	Average Splitting Stress	1.32
	Standard Deviation	0.05
	95 % confidence	0.04

3.3 Discussion of Results

3.3.1 *Quasi-Static Compressive Behavior*

From the trial and error approach adopted to obtain the right level of compaction to make specimens for quasi-static compression testing, there were three different specimens with three levels of compactions quantified by bulk specific gravity (method validated by Kim et al, 1997) as shown in Table 3.2. When these specimens were tested for quasi-static compressive behavior, the overall trend of the results (see Figs. 3.3-3.5) was similar. The figures illustrated five notable regimes:

1. An initial settling region
2. A linear portion (ascending branch) showing a constant rise to a peak stress value
3. A brief non linear portion of the ascending branch
4. A very short region of the peak stress value
5. A linear fall in strength of the material (descending branch) as the failure progresses

Table 3.2 Bulk Specific Gravity Values of Compression Testing Specimens

Amount of Compaction	Bulk Sp Gravity
80 Blows	2.320
90 Blows	2.380
Marshall Standard	2.300

Starodubsky et al (1994) have conducted a detailed experimental study to obtain stress strain relationship for asphalt concrete under short-term compression under the influence of various factors. Our stress-strain behaviors obtained in this study are similar to the results reported by Starodubsky; typically a smooth response composed of ascending and descending branches with a smooth transition between them. The five regions of stress-strain behavior observed in the present research are also reported in their study. It should also be noted that as expected, as the level of compaction increased, the peak compressive failure stress also increased.

3.3.2 *Failure Mode – Quasi-Static Compression*

Friction between the specimen and the loading platens plays a crucial role in compression testing of asphalt cement specimens. It is well known that, by inducing large lateral forces, the platens confine the specimen and prevent transverse Poisson extension of the specimen ends (Starodubsky et al (1994)). Effects of friction can be easily identified by looking at the way the

specimens failed. If friction was predominant, shear failure takes place as evident by inclined macro cracks. In the absence of friction, the specimens fail by vertical macro cracks (splitting). Fig 3.9 shows the failed specimens of quasi-static compression testing. As evident from these figures, friction effects were minimized and predominant failure was due to splitting. This would indicate that the layer of talc powder reduced the frictional effects.

3.3.3 *Quasi-Static Tensile Behavior*

The indirect tensile test (IDT) is widely accepted in the asphalt research community as a means to characterize the mixture. IDT is widely used as a method of evaluating the relative quality of materials as well as to generate input for pavement design or pavement evaluation and analysis. Force-extension curves of quasi-static IDT (Fig. 3.8) show typical trends of ascending and descending branches as seen in compression testing. However, the loads resisted are lower thus resulting in a tensile strength approximately 50% below compressive strength values.

3.3.4 *Failure Mode – Quasi-Static IDT*

Successful IDT splitting experiments are characterized by failure of the specimen along the centerline. A typical splitting event is shown in Fig. 3.10. As evident from the figure, failure does take place approximately along the centerline. Hence, the predominant resistance to failure is due to the tensile strength of the bituminous mix. Typical failure surfaces from a specimen are shown in Fig. 3.11. As seen, most of the failure paths were around the aggregates with minimal damage to aggregates. This would indicate that failure occurs in the binder and/or at the binder-aggregate interface bond. Although there was some small aggregate damage in regions near the contact area between specimen and loading strip, these effects do not contribute significantly to the overall sample damage behavior.

Fig. 3.1 Specimen photograph – quasi-static compression

Fig. 3.2 Setup for static compression testing

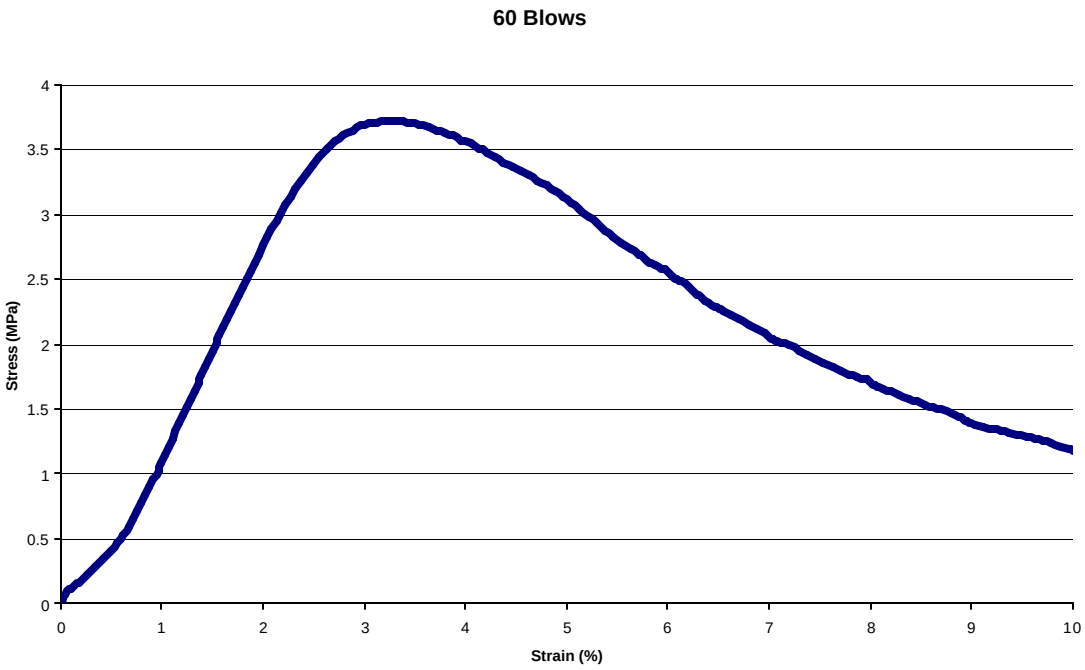

Fig. 3.3 Compression testing result of specimens compacted to 60 blows each end

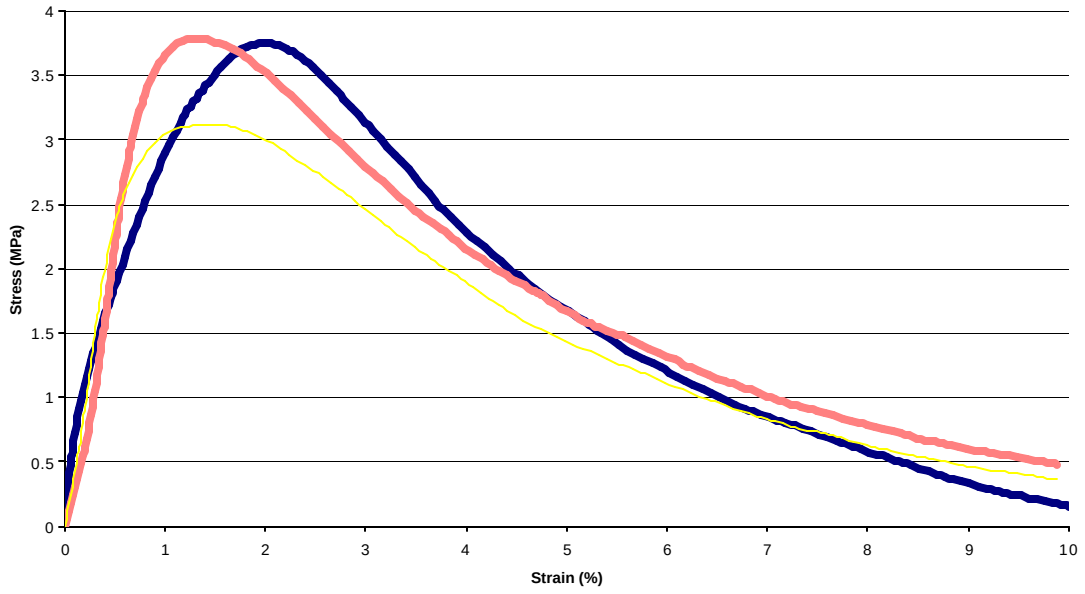

Fig. 3.4 Compression testing result of specimens compacted to 80 blows each end

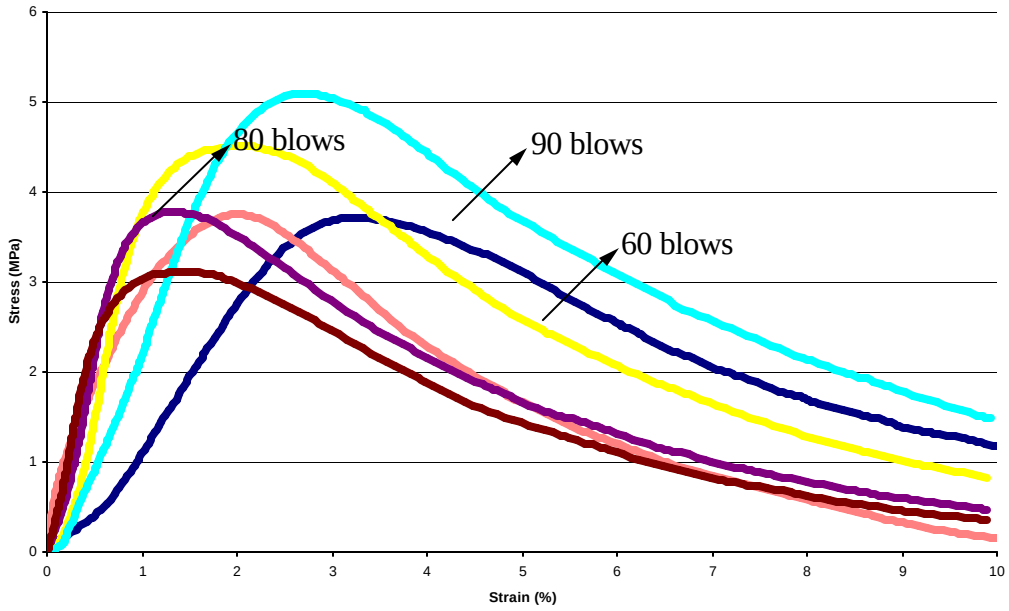

Fig. 3.5 Composite plot showing results obtained for different compaction levels

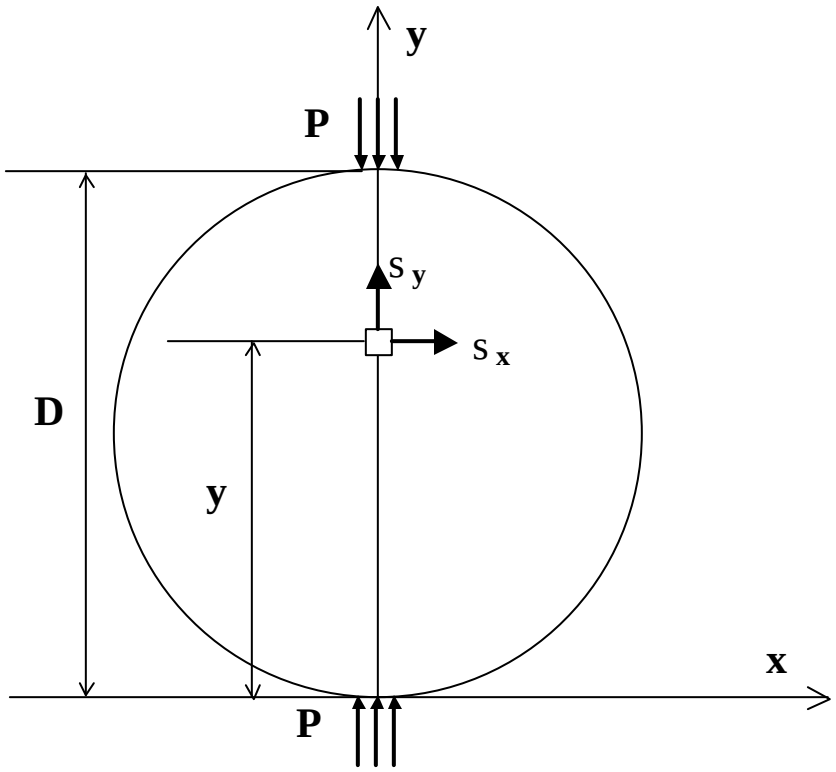

Fig. 3.6 A disk subjected to compressive loading

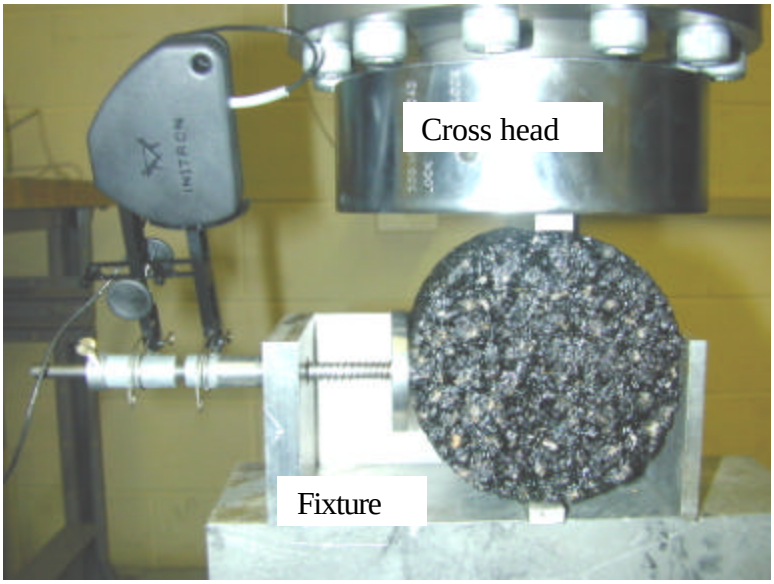

Fig. 3.7 Setup for quasi-static indirect tension test

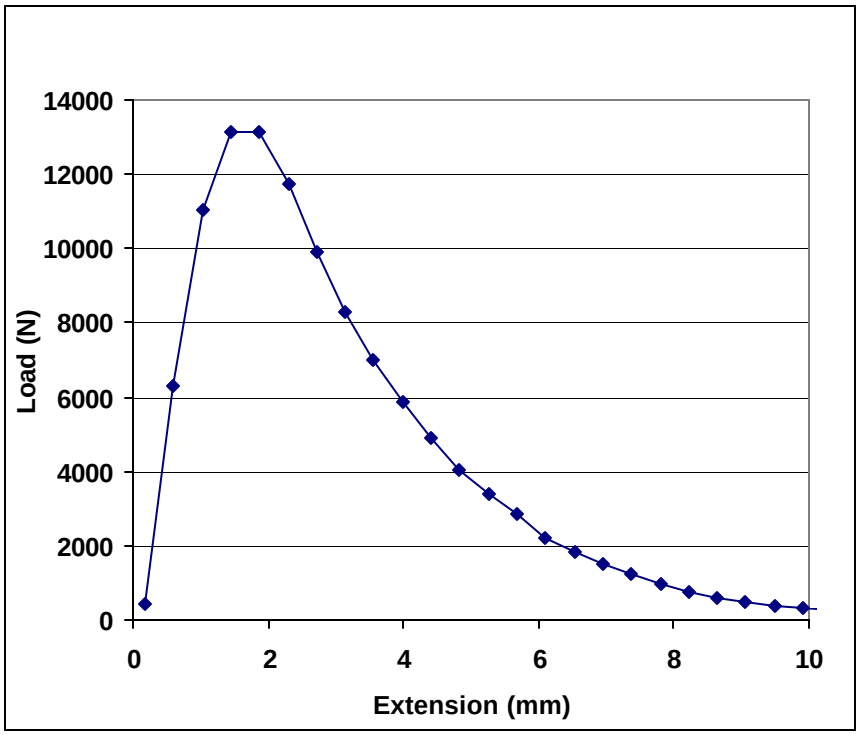

Fig. 3.8 Typical load-extension behavior of RAP under quasi-static indirect tensile test

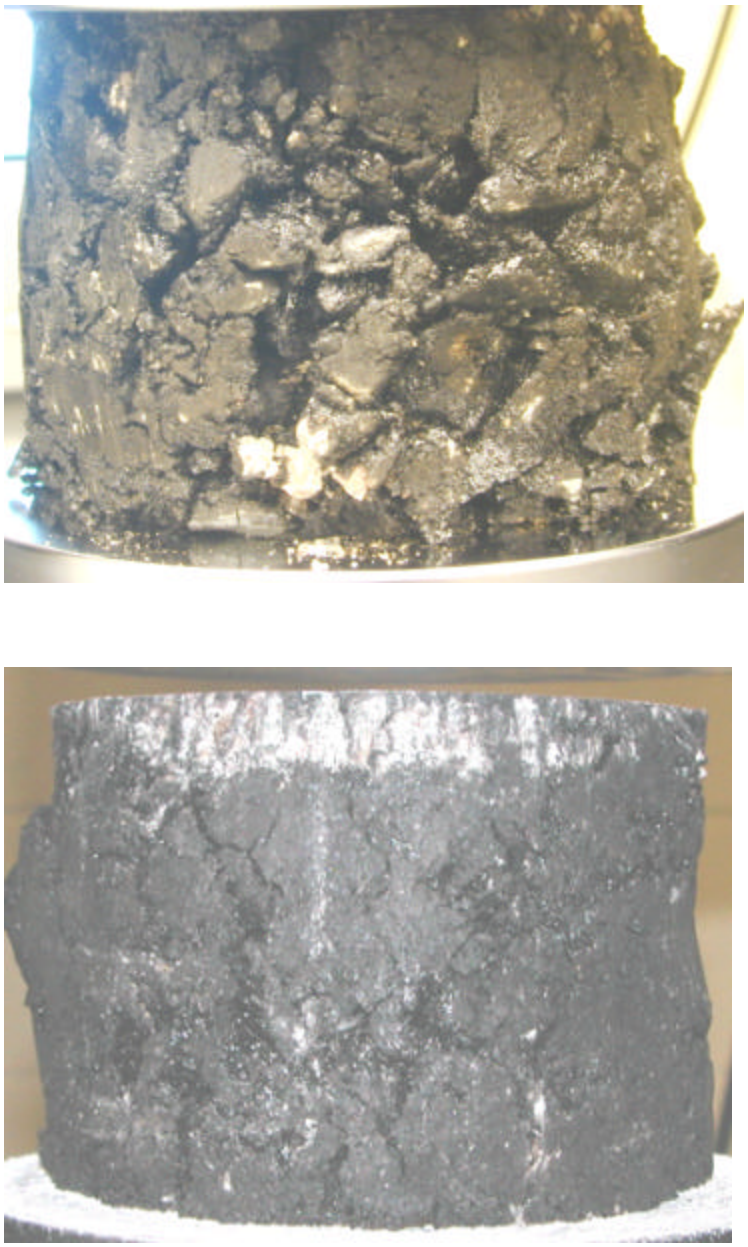

Fig. 3.9 Failed specimens from uniaxial compression testing

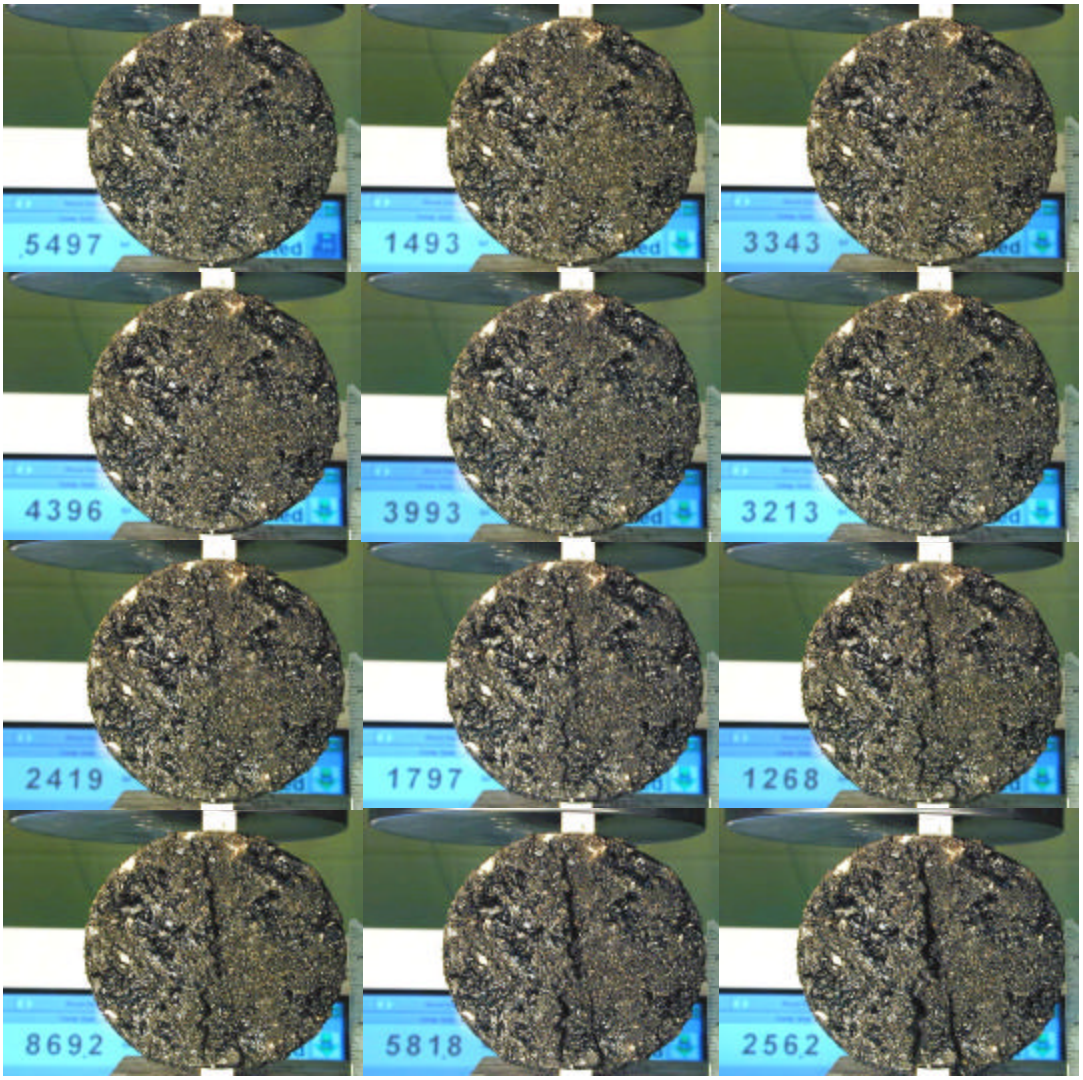

Fig. 3.10 Events to failure of quasi-static indirect tension testing
(Load readings (lb) are shown in inset)

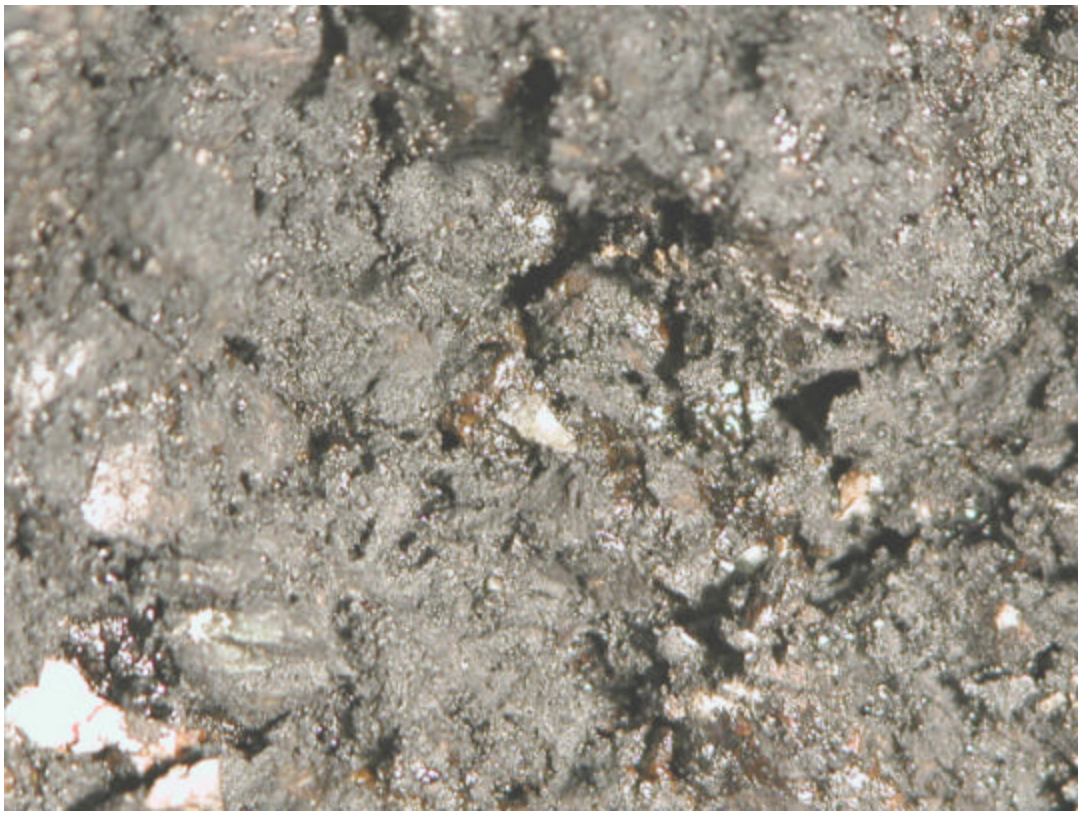

Fig. 3.11 Failure surface obtained by quasi-static indirect tension test

4. DYNAMIC CHARACTERIZATION

4.1 Introduction

Particular operating conditions can commonly lead to dynamic loading of pavement materials. Such cases may arise from an accident scenario whereby sizeable objects may be dropped on to structural pavement systems or from explosive devices. Other high rates of loading could come from high-speed traffic. It is well known that the behavior of asphalt concrete is highly rate dependent, and we certainly expect to see significant differences in the dynamic response when compared to quasi-static behavior. In particular we expect the stress-strain and fracture behaviors to be quite different for asphalt materials under dynamic loading conditions.

High strain rate data may be gathered using a variety of experimental methods depending on the test-piece size and the energy or velocity demands of the test. One scheme that has been used is the Charpy impact pendulum test, whereby an instrumented hammer is swung into a notched specimen. This gives rise to sample strain rates of $10\text{-}100s^{-1}$ with resultant impact energies of up to 600 joules. Another scheme has used drop-weight impact testing machines that develop similar strain rates but are capable of generating impact energies of 60,000 joules. At the other end of the spectrum are the Hopkinson Bars and Gas Guns that rely on force transmission by a gas pressure assisted rod or by actual projectile impact to achieve strain rates typically from $200\text{-}1000\ s^{-1}$. The Hopkinson Bar can develop energies of up to approximately 10 joules, while the Gas Gun can develop up to 600,000 joules. Our experimental program has used the Hopkinson Bar apparatus, and the basics of this method will be discussed in the next section. Note that conventional dynamic modulus testing of asphalt would generally be at least an order of magnitude slower than Hopkinson Bar testing.

4.2 Split Hopkinson Pressure Bar

The Hopkinson bar technique was first developed by John Hopkinson (1872) and Bertram Hopkinson (1914), who tried to characterize the dynamic response of metal wires and study the pressures produced due to impacting a long elastic bar. The displacements at the free end of a bar under impact were measured by R.M.Davies (1948). The present day setup having split bars was developed by Kolsky (1949), who sandwiched the specimen between the two split bars and hence the name Split Hopkinson Pressure Bar (SHPB) was coined. Harding et al developed the SHPB tensile gun and the use of strain gages to measure surface displacements. J.L Chiddester et al (1963) described a new method of performing high strain rate tests in

elevated temperatures. Baker et al (1966) described modified SHPB torsion tests in their work. Lindholm (1966) studied the annealed metals with FCC lattice, such as lead, Aluminum and Copper under uniform strain rates of 10^3 s^{-1} and developed a constitutive relationship over a range of strain rates from 10^{-4} - 10^3 s^{-1}. It was also the first time a continuous record of stress-strain data was made possible. Davies et al performed extensive SHPB tests on metals such as Aluminum, annealed Copper, Magnesium, Zinc and Brass and polymers such as PMMA, Polyethylene, PVC, etc., under dynamic compression and also derived a relation between the specimen geometry and Poisson's ratio to minimize inertial effects, inherent in the SHPB system.

In regard to cementous materials, Malvern et al (1985) applied the SHPB technique to dynamically characterize concrete and mortar. Direct tensile, splitting tensile and direct-compression tests of mortar and concrete were conducted at strain rates between 10 and 10^3 s^{-1} on the SHPB apparatus. Results from the study indicated the tensile strength of mortar to be 1.5 to 3 times that of the tensile strength at quasi-static strain rates. However, the dynamic tensile strength of concrete was found to be 4 to 6 times that under quasi-static conditions. Venkatram et al (1997) performed SHPB studies to determine the dynamic behavior of asphalt binder materials, and found significant differences in the dynamic response when compared to static behavior. These studies verified the applicability of the SHPB apparatus to determine the dynamic properties of mortar and concretes. Recent research using SHPB includes characterization of wide variety materials like composites, geo materials, polymers and metals under high strain rate loading. Researchers are now focusing on extensive numerical simulations of high strain rate loading events and the SHPB technique is used for verification and validation of these analyses.

Dynamic mechanical behavior of bituminous materials has received very little attention due to inherent difficulty in testing and interpretation of results. Therefore there exists a need to conduct such studies and determine the dynamic response of asphalt materials.

4.3 Theoretical Background

A conventional Split Hopkinson Pressure Bar consists of a striker bar, an incident bar and a transmitter bar, as illustrated in Fig. 4.1. The specimen under study is sandwiched between the incident and transmitter bar. The striker bar is launched at a predefined velocity towards the incident bar. This impact generates a compressive stress pulse that travels down the incident bar towards the specimen. The amplitude of the stress pulse is a function of the velocity of the striker bar, and its period is approximately equal to twice the travel time of the wave in the striker bar.

This wave, upon reaching the incident bar-specimen interface, gets partly reflected back and partly transmitted into the specimen depending on the impedance and area mismatch between the specimen and the bar. From one-dimensional wave theory, it has been established that the amplitude of the transmitted pulse is a function of the stress in the specimen, while the amplitude of the reflected pulse is a function of the strain rate in the specimen. Thus upon integrating the reflected pulse, the strain in the specimen can be determined. The specimen can be subjected to a wide range of strain rates by employing striker bars of various lengths.

The fundamental relations stem from the classical D'Alembert-one dimensional wave equation given by

$$u(x,t) = f(x - c_o t) + g(x + c_o t) \tag{4.1}$$

where f and g represent propagating disturbances determined by the initial conditions of the forcing function of a given problem. f corresponds to a wave traveling in the positive x direction while g corresponds to a wave traveling in the negative x-direction. The parameter c_o is the *wave speed* given by the relation $c_o = \sqrt{E_b / \rho}$, where E_b and ρ are the modulus of elasticity and density of the bar material. A schematic of the incident, reflected and the transmitted strain pulses, γ_i, γ_r, and γ_t are shown in Fig 4.1. From one dimensional rod theory, the displacements at the two specimen-bar interfaces are given by

$$u_1 = c_o \int_0^t (-\varepsilon_i + \varepsilon_r) dt \tag{4.2}$$

$$u_2 = -c_o \int_0^t \varepsilon_t dt \tag{4.3}$$

The average strain the specimen, γ_s, is then given by,

$$\varepsilon_s = \frac{c_o}{l_s} \int_0^t (\varepsilon_i - \varepsilon_r - \varepsilon_t) dt \tag{4.4}$$

where l_s is the length of the specimen. The loads at the two interfaces are given by,

$$P_1(t) = A_b E_b [\varepsilon_i(t) + \varepsilon_r(t)] \tag{4.5}$$

$$P_2(t) = A_b E_b \varepsilon_t(t) \tag{4.6}$$

where, A_b is the cross-sectional area of the bars. Now, an important assumption is made that wave propagation effects within the short specimen may be neglected, thus $P_1 = P_2$. From this, it follows that $\gamma_i + \gamma_r = \gamma_t$, and so,

$$\varepsilon_s(t) = \frac{-2\,c_o}{l_s}\int_0^t \varepsilon_r dt \tag{4.7}$$

The average stress in the specimen is given by,

$$\sigma_s = E_b \frac{A_b}{A_s}\varepsilon_t \tag{4.8}$$

where A_s is the instantaneous cross sectional area of the specimen.

4.4 Validity of Experimental Method

The validity of the previous equations is based on the following two fundamental assumptions.

(1) Wave propagation within the pressure bars must remain one-dimensional thus implying that surface measurements from the strain gages give the proper strain through the bar cross-section. A major of the wave energy is contained in wavelengths that exceed 10R where R is the radius of the bars. From wave theory, this implies that the motion can be assumed one-dimensional. When the $R/\lambda << 1$ or $R/\lambda < 0.1$, the surface displacements differ from the axial displacements by less than 5%, where λ is the wavelength of a pure cosine wave. Also, the stress pulses should suffer minimal dispersion, which arises due to variation of the longitudinal velocity in the bar with respect to the wavelength. These oscillations lag behind the leading edge of the wave and have only a minor influence on the stress-strain behavior predicted for the specimen.

(2) The specimen must undergo homogenous deformation. Uniform deformation is generally hindered by radial and longitudinal inertia of the specimen and the frictional contact at the specimen-bar interfaces. Hence, it is customary to use oil-based molybdenum di-sulphide as a lubricant for experiments conducted at room temperature.

Accelerations both in the longitudinal and radial directions can be observed in a specimen under the action of a stress wave passing through it. It has been estimated that the stress wave

takes about π reverberations to equilibrate in a specimen deforming plastically. The time taken from Taylor Von Karman theory is given by,

$$t = \sqrt{\frac{\pi^2 \rho_s l_s^2}{\frac{d\sigma}{d\varepsilon}}} \tag{4.9}$$

where, ρ_s is the density of the specimen, l_s is the length of the specimen and $d\sigma/d\gamma$ is the slope of the true stress-strain curve.

It is in this regard that it the knowledge of the shape of the pulse becomes overriding. The time for equilibrium as mentioned above, becomes significantly lessened if trapezoidal pulses are obtained as the stress build up at both the specimen-bar interfaces becomes uniform and regular. However, with triangular pulses, the stresses will remain non-uniform and irregular for a considerable period of time, within which useful data may have to be disregarded due to its invalidity. Another method that is frequently used to yield valid data early in the strain history is to increase the rise time of incident stress wave. This procedure is known as pulse shaping, where a soft deformable disc is placed at the impact end of the incident bar. The choice of the material for the disc depends on the strain rate of the experiment and the strength of the specimen. Usually, the disc is made of the same material as the specimen and its thickness is varied between 0.1 mm to 0.2 mm. It should however be noted that by incorporating the deformable disc the obtainable strain rate from the experiment is reduced.

The predicted stress-strain behavior when the specimen is deforming uniformly can still be affected by longitudinal and radial inertia. Davies and Hunter (1963) predicted that the errors due to inertia will be minimized by holding the strain rate constant, which can be accomplished by choosing the specimen dimensions that conform to the following equation,

$$\frac{l_s}{D_s} = \nu_s \sqrt{\frac{3}{4}} \tag{4.10}$$

where D_s and ν_s are the specimen diameter and Poisson's ratio. This correction has been incorporated in the design of the specimens used in this study.

As has been previously mentioned friction poses considerable problems in the interpretation of the stress strain data obtained. Lack of lubrication may cause the measured values of stresses to be higher than the actual values due to non-uniform sample deformation. This phenomenon can occur both under quasi-static and dynamic loading.

4.5 Dynamic Compressive Behavior

The specimen geometry used in dynamic compression testing was a cylindrical specimen of diameter 1.9 inch and thickness of 0.5 inch as shown in Fig. 4.2. A minimum of five tests was performed on compression SHPB with the specimens sandwiched between the bars as shown in Fig. 4.3. The specimen ends were made flat and smooth to have complete contact with the bar, and a thin layer of lubricant was used to minimize the frictional effects. The strain-time history recorded by axial strain gages were recorded and post processed using an in-house MATLAB program.

Results obtained from four tests are shown in Fig. 4.4 where plots of the true stress vs. true strain are drawn. It is observed that some variation exists in the magnitude of the dynamic compressive peak stress. From the figure, we can state that bituminous mix with 30% RAP has a peak failure stress in the range 15-25 MPa at a corresponding strain of 0.01-0.015.

4.6 Dynamic Indirect Tension Testing

IDT (tensile splitting) experiments were conducted in the SHPB apparatus. In the dynamic tests, there are concerns about the validity of static equations being applied to dynamic loading using SHPB and equilibrium being attained in the specimen. Gomez et al (2001) have performed photo elastic experiment in a brittle material to observe the stress field development during dynamic loading, to verify if the loads calculated from the SHPB strain gages are accurate and to determine whether the specimen was under equilibrium. Their experiments proved that equilibrium was attained and that strain gage data is reliable.

In order to perform the tensile splitting experiments under dynamic loading in the SHPB apparatus, the specimen is held diametrically between the bars using steel bearing pads to avoid localized failure at the loading points. To load the specimen, the incident bar is impacted with a projectile fired from a gas gun, which creates a compressive wave traveling down the bar. At the specimen, this wave is partially reflected back into the incident bar and partially transmitted through the specimen into the transmitter bar. Strain gages mounted at the midpoints of both the bars are used to record the strain waves. Assuming one dimensional wave propagation, and negligible wave attenuation, the loads on each end of the specimen are given by

$$P_1(t) = A_b E_b [\varepsilon_i(t) + \varepsilon_r(t)] \tag{4.11}$$

$$P_2(t) = A_b E_b \varepsilon_t(t) \tag{4.12}$$

where P_1 and P_2 are the loads on the incident and transmitted bar contact faces, and the incident, reflected and transmitted strains have been shifted in time to account for the mid bar location of the strain gages.

For specimens in compression, the SHPB analysis assumes that the load on each specimen face is equal, so that the specimen is in equilibrium. With this assumption, the specimen stress/strain response can be obtained. However, for the dynamic splitting, the standard analysis to obtain the specimen stress can no longer be used. For these experiments, it has been assumed that the peak tensile splitting stress of the cylinder is proportional to the peak transmitted compressive strain measured in the transmitter bar, and that the load P is given by

$$P_{\max} = \pi R_{bar}^2 E_{bar} \varepsilon_t^{\max} \tag{4.13}$$

where R_{bar} and E_{bar} are the transmitter bar radius and Young's modulus respectively, and $\varepsilon_t^{\max}$ is the maximum strain measured in the transmitter bar.

The conventional SHPB apparatus made of hardened steel bars was used to perform the indirect tensile test on our asphalt samples. Since the impedance mismatch between hardened steel and bituminous materials is so large, the transmitted signal obtained was found to be too small as shown in Fig. 4.5. As seen in the figure, there was effectively no noticeable differentiation between the signal and inherent noise present in the system. So the conventional method had to be modified for practical use to test bituminous materials. Chen et al (1999) proposed a modification to conventional SHPB for measuring the compressive stress strain behavior of materials with low mechanical impedance. They suggested the use of a more compliant bar by either changing the material or cross-section. Analysis using a hollow tube instead of a solid transmission bar indicated that there would be approximately an increase in the transmitted strain by a factor of 12.

Considering the wave propagational characteristics of the two bar system shown in Fig. 4.6, we can define the two materials with subscripts 1 and 2 as shown. The *impedance ratio* can then be defined by

$$\mu = \frac{(\rho c)_1}{(\rho c)_2} \tag{4.14}$$

where ρ = density of the material and $c = \sqrt{E/\rho}$ = wave propagation speed in the material. If μ = 1, there will be no reflected pulse and complete transmission with all energy going through the sample. However, if the impedance ratio is very large, then very little energy will be transmitted through the sample.

As a modification for testing asphalt materials, an incident bar of solid steel and a transmitted bar of hollow aluminum tube with wall thickness of 1/8" (3.175mm) was tried. For such a system made of (1)steel and (2)aluminum, we can obtain, c_{St} = 5063m/s; c_{Al} = 4964m/s; and thus μ = 2.842. From simple wave analysis (Sadd, 2000), the stress ratio are given by

$$\frac{\sigma_r}{\sigma_i} = \frac{1-\mu\dfrac{A_1}{A_2}}{1+\mu\dfrac{A_1}{A_2}} \tag{4.15}$$

$$\frac{\sigma_t}{\sigma_i} = \frac{2\dfrac{A_1}{A_2}}{1+\mu\dfrac{A_1}{A_2}} \tag{4.16}$$

where σ_i = the incident stress, σ_r = the reflected stress, and σ_t = the transmitted stress. For a solid incident bar with diameter of 2 inch and hollow tube of OD = 2" and ID=1.75", the area ratio is determined as A_1/A_2 = 4.29, and we find that the stress ratios become

$$\frac{\sigma_r}{\sigma_i} = -0.849 \quad \frac{\sigma_t}{\sigma_i} = 0.650 \tag{4.17}$$

With known values of E_{St} = 200 GPa and E_{Al} = 69 GPa, the strain ratios become

$$\frac{\varepsilon_r}{\varepsilon_i} = -0.849 \quad \frac{\varepsilon_t}{\varepsilon_i} = 1.884 \tag{4.18}$$

which again proves that the transmitted signal is stronger in the aluminum tube than in solid steel bar. The above analysis provides the calibration method for the new setup and the validity of the experimental pulses can be checked using these relations.

Calibration experiments were done to verify that the modification was justified. A blank shot was fired and the strain gages on incident and transmitted bar measured the strain pulses.

The incident strain pulse was observed to be 538 micro strain. From theory, the reflected and transmitted strains were calculated to be, ε_r = 456 micro strain and ε_t = 1014 micro strain. Corresponding values obtained from the experiment where found to ε_r = 448 micro strain and ε_t = 890 micro strain. A typical strain-time plot showing these results is shown in Fig. 4.7. As seen in the figure, the theoretical and experimental values match closely. With this successful calibration, we proceeded to use a hollow aluminum transmission bar in the modified SHPB testing apparatus for testing bituminous materials.

Test methods for the splitting tensile strength of concrete and rock are specified by ASTM standards C496 and D3967. For asphalt materials, these same standards have been used, and a typical specimen and setup is shown in Fig. 4.8. A special fixture was designed and made to hold the specimen in balance while placing them between the bars. The tests were performed on a standard SHPB apparatus with samples loaded along the diameter in the usual manner. Strain gages on the transmitted bar recorded strain time history, and this data was post-processed to obtain the force time history. The maximum recorded force in the transmitted bar was used to calculate the dynamic splitting stress using the static relation given in relation (3.1). A typical plot of the recorded strain data is shown in Fig. 4.9. Seven tests were performed under dynamic splitting, and the results are shown Table 4.1. Figure 4.10 shows the splitting stress corresponding to the rate of stress applied to the specimen, and these results gave an average splitting stress of 1.53 MPa.

4.7 Discussion of Results

The dynamic IDT results shown in Fig. 4.10 indicate that the splitting stress increases slightly with stress rate. When compared to the quasi-static case, the dynamic splitting stress results were about 16% higher. In regard to failure, IDT splitting occurred approximately along the loaded centerline as shown in Fig. 4.11. Some of these failure surfaces were carefully observed after the test. Figure 4.12 shows one such IDT failure surface, and it was found that several aggregates were fractured. Thus for the dynamic case, we conclude that in addition to binder failure, considerable trans-aggregate fracture has also contributed to the overall sample failure and fracture toughness.

For the dynamic compression tests, the overall stress-strain response was given by Fig. 4.4. Typical failure modes of the compression samples are shown in Fig. 4.13. Post mortem analysis revealed that the dominant failure mechanism was multiple fracture into several pieces that included failure of binder as well as aggregate. Such a failure is typical for rock and

concretes, and results in a large increase in the material's resistance to failure. This is reflected in the large increase in the overall dynamic failure stress, which was about five times quasi-static value.

Table 4.1 Results from Dynamic Indirect Tensile Testing of Bituminous Mix with 30% RAP

Test No.	Peak Transmitted Force (kN)	Dynamic Splitting Stress (MPa)
1	11.41	1.41
2	11.67	1.44
3	11.86	1.46
4	12.66	1.56
5	12.48	1.54
6	14.27	1.76
7	12.43	1.53
	Average	1.53
	Standard Deviation	0.12
	95 % confidence	0.09

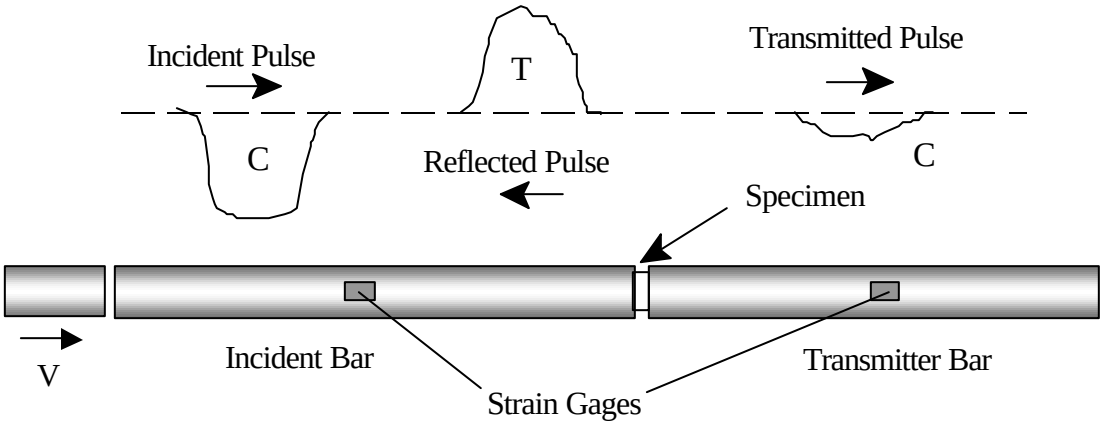

Fig. 4.1 SHPB apparatus and typical pulses obtained in testing

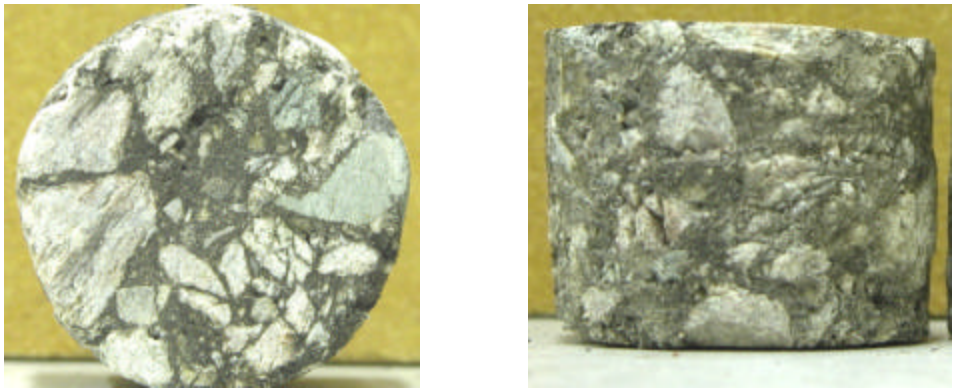

Fig. 4.2 Typical specimens used for dynamic compression test

Fig. 4.3 Dynamic compressive testing setup with specimen between bars

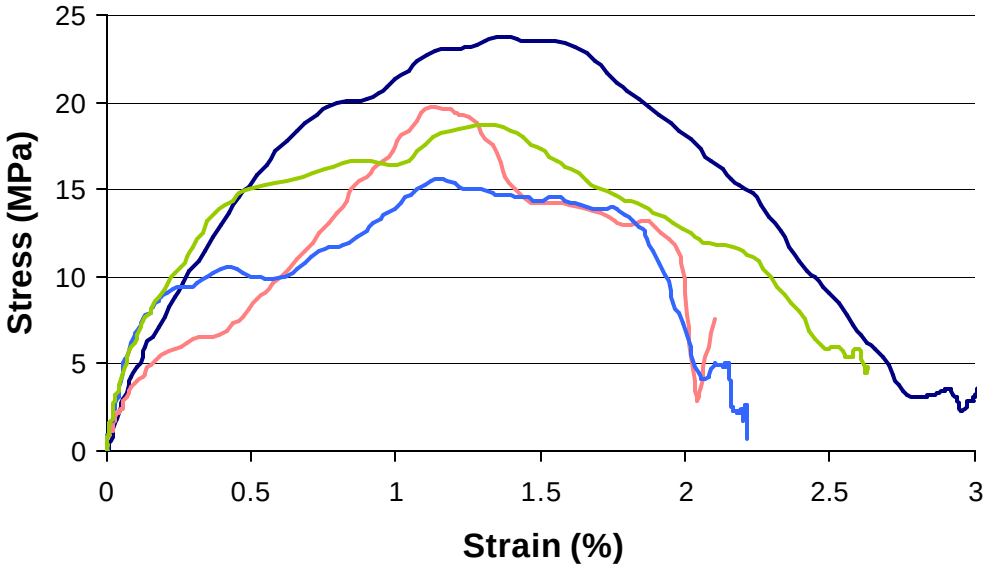

Fig. 4.4 Dynamic compression stress-strain behavior of asphalt samples

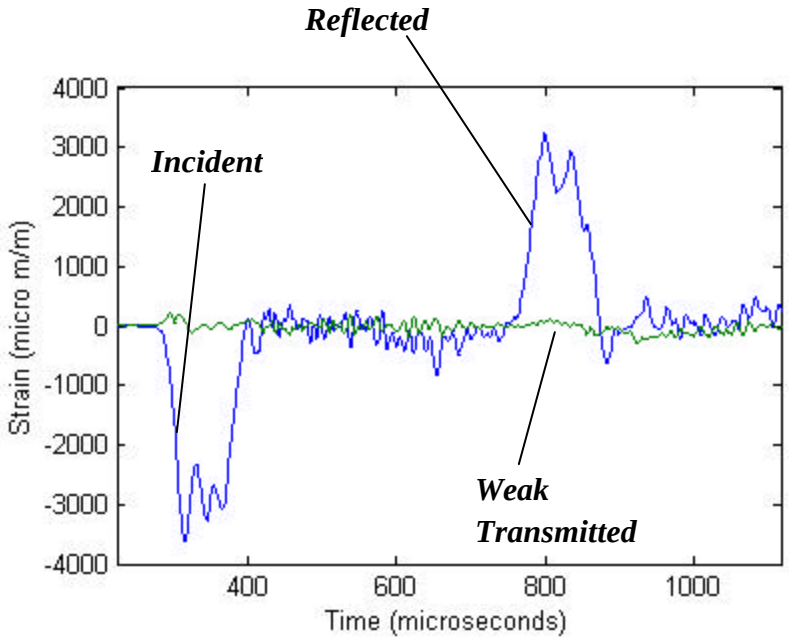

Fig. 4.5 Typical pulses obtained using conventional SHPB for asphalt IDT samples

Fig. 4.6 Two material system under one-dimensional wave propagation

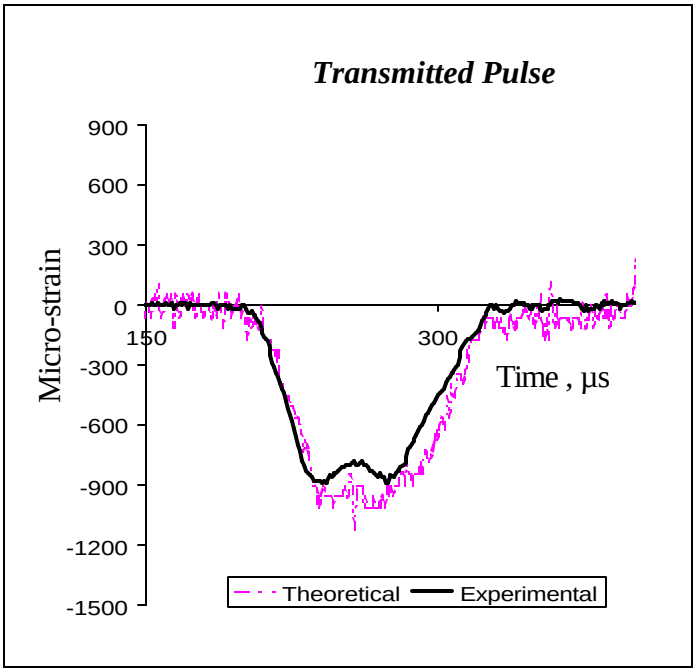

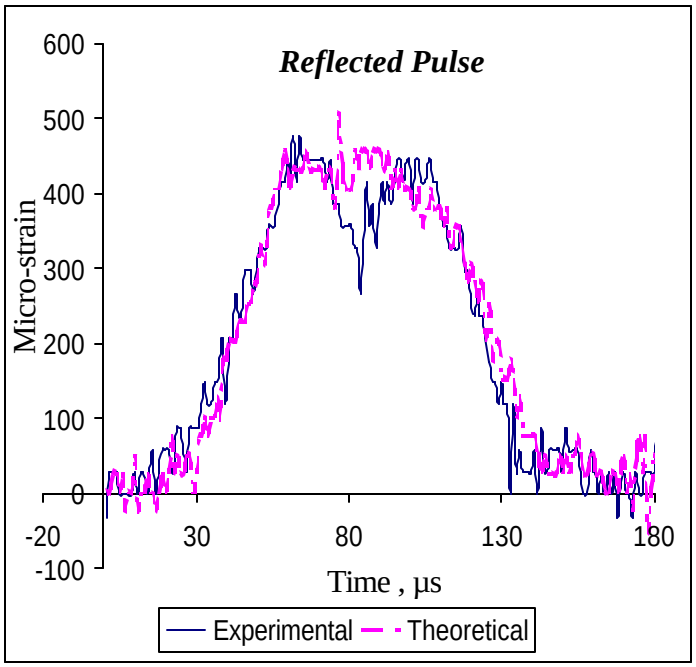

Fig. 4.7 Calibration of modified SHPB for IDT testing of bituminous material

Fig. 4.8 Dynamic indirect tensile test setup in SHPB apparatus

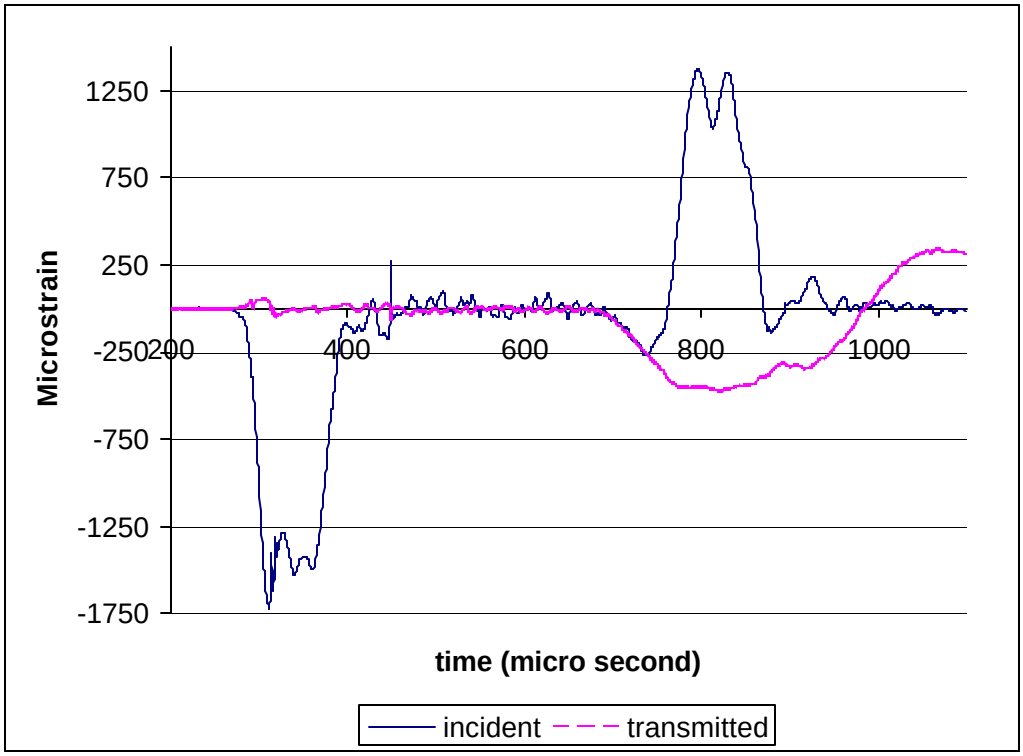

Fig. 4.9 Typical pulses obtained using modified indirect tension SHPB

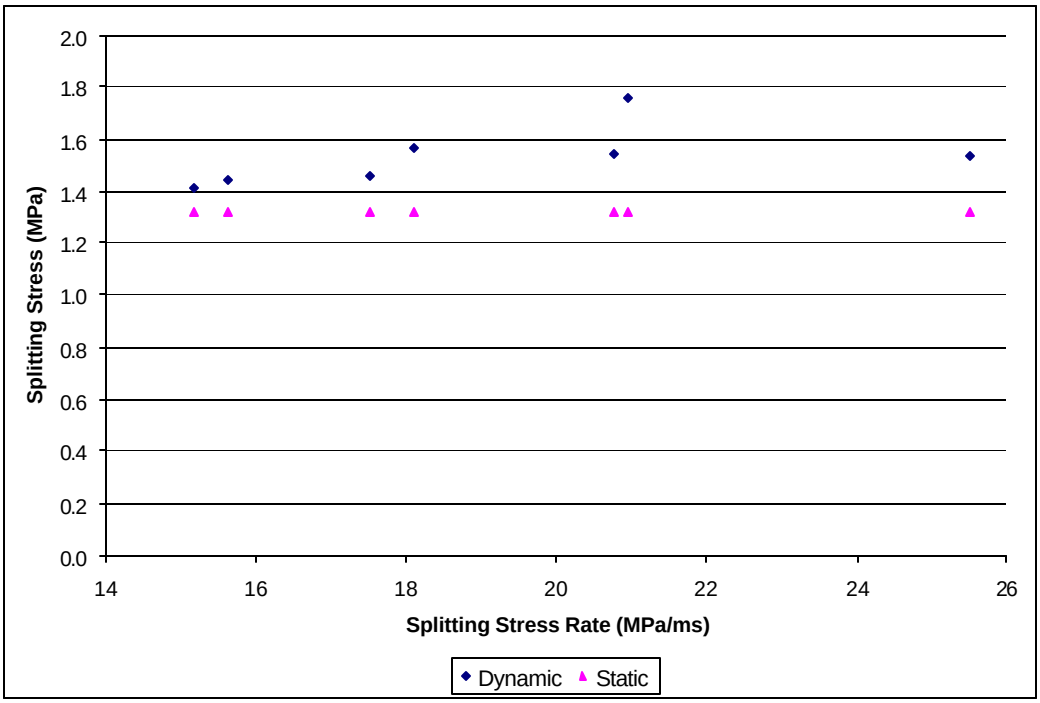

Fig. 4.10 Dynamic splitting stress behavior of asphalt samples

Fig. 4.11 Typical splitting failure in dynamic IDT testing

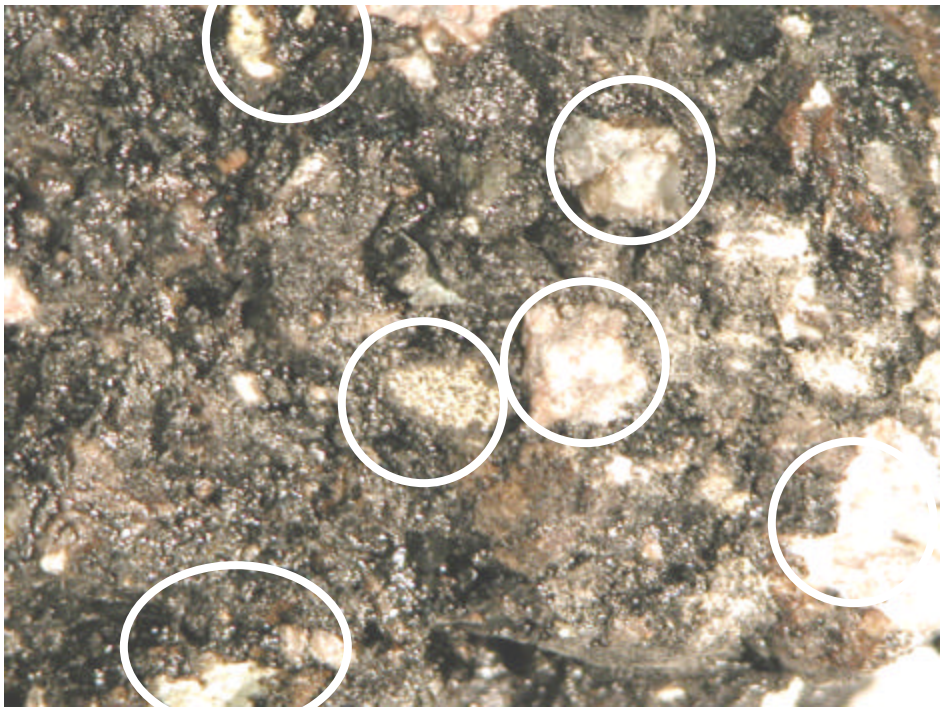

Fig. 4.12 Failure surface from dynamic indirect tension testing
(fractured aggregates marked with circles)

Fig. 4.13 Failure pattern from dynamic compression testing
(fractured aggregates marked with circles)

5. FRACTURE TOUGHNESS TESTING

5.1 Fracture Mechanics

Linear elastic fracture mechanics (LEFM) is the theoretical foundation of the fracture of solids. Over the years various theoretical advancements have extended this theory to account for various types of non-linear material behavior. The elastic stress field near the tip of a general crack may be formulated in terms of parameter called the *stress intensity factor*, K_I (opening mode). In structural mechanics it is well known that fracture behavior can be quantified in terms of this parameter. The stress intensity factor is related to the level of stresses near the crack tip, and when this factor exceeds the limit state, i.e. the critical value K_{Ic}, fracture can be expected to occur. This critical value is commonly referred to as the *fracture toughness* of the material. The property K_{Ic} characterizes the resistance of a material to fracture for the case of linear elastic behavior under plane strain conditions, and can also be used for materials with inelastic behavior if the non-elastic crack tip zone is small compared to the sample size. Fracture toughness testing is normally conducted on standardized samples whereby measurements on the fracture load will allow K_{Ic} to be determined.

Three modes of fracture are normally defined as shown in Fig. 5.1. Of these, mode I is the most related to material failure, and thus this research is primarily focused on mode I fracture characterization. For an infinite plate with a crack, as shown in Fig. 5.2, the stress intensity factor is given by

$$K_I = \sigma\sqrt{\pi a} \tag{5.1}$$

Failure is said to occur when $K_I = K_{Ic}$, and hence the stress intensity factor is the driving force for fracture and K_{Ic} is a measure of material resistance to fracture. Solutions from theory of elasticity for K_I are well developed for various geometries and loading configurations used in laboratory testing.

5.2 Specimen and Testing Geometry

There is no prescribed ASTM standard for testing fracture toughness of bituminous materials, and thus we considered several possible geometries and loading conditions for our particular testing program. A literature review indicated that ASTM D 5045 is a standard three-point bend test prescribed for plastic materials and that this geometry would also be appropriate for bituminous materials. Kim and El Hussein (1997) have also used this geometry for studying

the fracture behavior of asphalt materials. The *three-point bend* or *single edge notched beam* (SENB) configuration is shown in Fig. 5.3. Solutions for K_I for the geometry in Fig 5.3, have been given by Anderson, 1995 as

$$K_I = \frac{P\, f(a/w)}{B\sqrt{w}} \tag{5.2}$$

where the various parameters are defined in Fig. 5.3, and $f(a/w)$ is a dimensionless geometry factor obtained from standard stress analysis methods and is given by

$$f(a/w) = \frac{3\frac{S}{w}\sqrt{\frac{a}{w}}}{2\left(1+2\frac{a}{w}\right)\left(1-\frac{a}{w}\right)^{3/2}}\left[1.99 - \frac{a}{w}\left(1-\frac{a}{w}\right)\left\{2.15 - 3.93\left(\frac{a}{w}\right) + 2.7\left(\frac{a}{w}\right)^2\right\}\right] \tag{5.3}$$

Two different specimen geometries were used in the testing program. The first type, which we call "large" beams, had a *S/w* ratio of 2.2. The second type, which we call "small" beams, had a *S/w* ratio of 4.4 (following ASTM D 5045). These two specimens are shown in Fig. 5.4, and their dimensions are as follows:

Large Beams

L = 12" (305mm), S = 8.8" (223.5mm), w = 4" (101.6mm), a = 2" (50.8mm), B = 2" (50.8mm) which gave $f(a/w)$ = 5.82.

Small Beams

L = 12" (305mm), S = 8.8" (223.5mm), w = 2" (50.8mm), a = 1" (25.4mm), B = 2" (50.8mm), which gave $f(a/w)$ = 11.64.

The cracks in the specimen were sharpened using a handsaw and the procedure was maintained uniform in all the specimens to ensure repeatability. The sample was placed in a special testing fixture and loaded through a roller directly above the crack as shown in Fig. 5.5

5. 3 Quasi-Static Testing and Results

Quasi-static fracture toughness testing was done on an Instron universal testing machine. A vertical cross head displacement of 5.08 mm/min (0.2 inch/min) was used for testing the SENB specimens. The testing machine continuously recorded the load and vertical deformation of the

sample, and a typical load-deformation plot is shown in Fig. 5.6. This data was post processed to obtain the peak load and this was used in subsequent calculation of K_{Ic} values using a simple MATLAB program incorporating relations (5.2) and (5.3). Table 5.1 summarizes the values obtained for K_{Ic} for the large beams. Table 5.2 summarizes similarly the results obtained for small beams. An average value of 0.23 MPa√m was obtained as K_{Ic} for the large beams, while corresponding value for small beams was 0.11 MPa√m.

Table 5.1 Results of fracture toughness testing of large beams

Test No	K_{IC}(MPa√m)
1	0.216
2	0.235
3	0.248
Average	0.233
Standard Deviation	0.016
95 % Confidence	0.018

Table 5.2 Results of fracture toughness testing of small beams

Test No	K_{IC}(MPa√m)
1	0.110
2	0.112
3	0.113
Average	0.112
Standard Deviation	0.001
95 % Confidence	0.001

5.4 Dynamic Fracture Studies

Dynamic fracture toughness is a measure of material fracture resistance at high loading rates. In such situations, inertia effects and material rate dependency are significant factors. Instrumented impact tests, such as the Charpy test, have been employed to determine dynamic fracture toughness. These striking hammer-type techniques however, possess their own shortcomings, such as oscillations in the load-time profile and loss of contact between the

specimen and the supports. Alternative methods have been used to circumvent these problems. Some of these alternative methods involve the use of unsupported bend specimens (1PB specimens) as a way of obtaining smoothly varying stress intensity factors.

Under quasi-static loading conditions the stress-intensity factor is directly proportional to the applied force, and subsequent determination of fracture toughness is generally straightforward. Under dynamic loading conditions the aforementioned proportionality between stress-intensity factor and applied force using the 3PB specimen is compromised due to material inertia effects, rendering interpretation of final results difficult. Traditionally, researchers have circumvented the inertia problem by calculating the stress-intensity factor from local measurements of stress field near the tip of the crack using strain gages and optical techniques. More recently researchers have relied on dynamic measuring procedures that have their roots on measurements of equivalent static values. In this approach the dynamic load history is measured, and the initiation toughness is calculated from the fracture load using static relations. Though easier to apply, these procedures have limitations on the applicable range of the test. They essentially require an increase in the time to fracture of the specimen so that quasi-static conditions prevail, and thus static relations apply. For relatively low impedance materials such an increase can be achieved by a reduction in the loading rate of testing, and/or by using a low impedance incident bar material (such as a polymeric) in the SHPB apparatus.

The use of polymeric incident bars in SHPB experiments presents its own set of challenges. First, care must be taken to ensure that the yield stress of the bar and projectile is not exceeded, as linear elastodynamics is the foundation of relations used in the determination of load point force. Secondly, a close-to-perfect impact between the projectile and the bar is crucial, as improper unloading of the reflected wave in the projectile during separation from the bar can cause a low amplitude trail to be generated in the main pulse in the incident bar. The ensuing loss of definition of the incident pulse, and ultimately of the reflected pulse, makes it difficult to correctly locate the beginning of the reflected pulse when adding the two pulses in accordance with relation (5.1). All other factors being equal, the pulse generated in a polymeric bar has a longer rise time than that generated in its metallic counterpart. Thus, care must be taken to ensure that the bar is long enough so that there is no overlap of the incident and reflected waves at the gage location.

Dynamic fracture toughness of bituminous materials is a relatively new concept and hence no standard test method exists. In order to facilitate comparison with the static values and

to follow the validated method of Evora and Shukla (2003), the same specimen geometry was used as that for the small beams in the static fracture toughness.

A *Modified Hopkinson Pressure Bar* (MHPB) apparatus was used to load the three point bend specimens to dynamic failure as shown in Fig. 5.7. The apparatus consisted of a 2.3m long, 12.7mm diameter polycarbonate (LEXAN) incident bar (1470m/s longitudinal wave speed). The projectiles used were also made from LEXAN and were 12.7mm in diameter. Projectile length was 610mm; long enough to avoid dispersion and also ensure a steady loading rate. The cylindrical projectile was propelled down the barrel of a gas gun using compressed air. Upon impact with the incident bar, a compressive pulse was generated which traveled down the bar toward specimen. Upon reaching the specimen, the impact force of the pulse was transmitted to the specimen and ultimately loaded the crack tip. Incident and reflected strain-pulse histories were obtained from two strain gages (EA-13-060LZ-120, Micro Measurements, Inc.) diametrically located at the midpoint of the bar. Strain gage signals were demodulated using Ectron 563F signal conditioners, and were subsequently recorded on a LeCroy 8025 data acquisition system. Signals from the gages were averaged to eliminate bending strains. The projectile and bar were made from the same material so that a well-defined single pulse could be generated. A thin sheet of cardboard was placed between the projectile and the bar to reduce high frequency components generated in the incident pulse during impact, and also to increase the rise time of the incident pulse. Since the diameter of the bar (1/2in) was less than the thickness of the beam (2in), special alignment marks were used to ensure the dynamic loading was applied to the center of the fracture specimen. Additionally, the loading end of the incident bar was rounded off slightly to more closely simulate single point contact with the specimen.

Strain gages on the MHPB apparatus recorded the strain time profiles of incident and reflected pulses, and this data was post processed to obtain force-time on history applied to the specimen by employing equation (4.5). If the time to fracture is allowed to be sufficiently long by decreasing the impact velocity and/or employing a low impedance incident bar, inertia effects can be neglected, and quasi-static analysis can be used (Martins and Prakash, 2002). For the SENB specimen, the static mode-I (opening mode) relations (5.2) and (5.3) can be used to calculate the stress intensity factor history with the loading being a function of time, i.e. $P = P(t)$. The dynamic fracture toughness then corresponds to the value of stress intensity factor at the time of crack initiation, i.e.,

$$K_{ID} = K_I(t_{init}) \tag{5.4}$$

It was observed that the time of crack initiation corresponded to the time of peak loading attained in the specimen. Experimental verification of these procedures was initially developed by Evora and Shukla (2003). Typical strain-time profiles are shown in Fig. 5.8, and the corresponding force-time profiles of the specimen are shown in Fig. 5.9. The dynamic stress intensity factor, $K_I(t)$ is plotted versus time in Fig. 5.10, and the average K_{ID} value was found to be 2.0MPa$\sqrt{}$m.

5.5 Discussion of Results

5.5.1 *Quasi-Static Fracture Toughness*

Linear Elastic Fracture Mechanics (LEFM) is the foundation of plane strain fracture toughness testing of brittle materials adopted as the method in this study. Since the binder seldom behaves as a perfect brittle material under ambient temperature (25 deg C), there are very few instances of research involving fracture toughness study of asphalt materials at room temperature. Kim et al (1997) have experimentally evaluated the fracture toughness of asphalt concrete mixes at low temperature ranging from –5 to –30 deg C. To account for non-linear behavior, they have developed the concept of Effective Crack Model (ECM) and hence their method of K_{Ic} evaluation differs considerably from the present study. Various asphalt research groups have developed methods to characterize bituminous mix fracture toughness. Still there is no present consensus or standard on fracture toughness testing of these materials. The three-point bend method is widely accepted as test method to obtain load-deflection behavior of notched beams of asphalt mixes. Typical load deflection curves (Fig. 5.6) confirm well with the observed trends for asphalt mixes obtained by other researchers Kim (1997,1999) and Barzin Mobasher et al (1997). The results of the critical stress intensity factor (K_{Ic}) shows that as beam thickness increases, the fracture toughness also increases (holding all other geometrical dimensions the same). This matches with similar results obtained by Evora and Shukla (2003) for brittle materials.

A typical crack face and fractured surface is shown in Fig. 5.11. As evident from the figure, the crack propagated only through the binder material and thus the effect of the aggregates appears to guide or redirect the path of failure. The resultant low values of K_{Ic} reflect this idea. Previous studies on binders by S Venkatram et al (1997) have shown typical virgin binder K_{Ic} values of 0.029 MPa$\sqrt{}$m under a loading rate similar to that used in the present study.

Values of K_{Ic} obtained in this study (0.11 MPa$\sqrt{m}$) are higher than the virgin binder toughness by a factor of about 3. This increase is attributed to presence of aggregates which provides an increase in fracture resistance due to failure path redirection. Studies on strengthening of binder on fracture toughness were performed by Hesp et al (2002) under low temperature (-28 to –34 deg C). Typical K_{Ic} values were 0.102-0.107 MPa$\sqrt{m}$ for the same binder used in this study but with polymeric modifiers. This further suggests that the K_{Ic} values obtained in this study are indeed representative of fracture toughness, to a certain extent of approximation on material brittle behavior. The authors also feel that further extensive research is needed on procedures and parameters for room temperature study of fracture toughness of bituminous materials.

5.5.2 ***Dynamic Fracture Toughness***

Figure 5.12 shows a typical dynamic test resulting in fracture of the specimen by the impact of bar. A typical postmortem examination of a fractured sample is shown in Fig. 5.13, and this reveals details on the crack faces and fractured surfaces of the beam specimen. It is evident from the figure that for dynamic loading several of the aggregates have fractured. Broken surfaces of coarse aggregates are clearly visible, and this behavior is quite different from the shear binder failure in the quasi-static fracture studies. Thus similar to our previous dynamic IDT studies, trans-aggregate failure has taken place and this offers considerable resistance to the fracture, and thus explains the increase in the critical stress intensity factor. It is therefore concluded that the increase in K_{Ic} is due to the following factors:

(1) Trans aggregate failure and hence contribution to fracture toughness

(2) Material stiffening, which includes binder and aggregates individually as well as the whole mix behavior when subjected to high strain rate loadings.

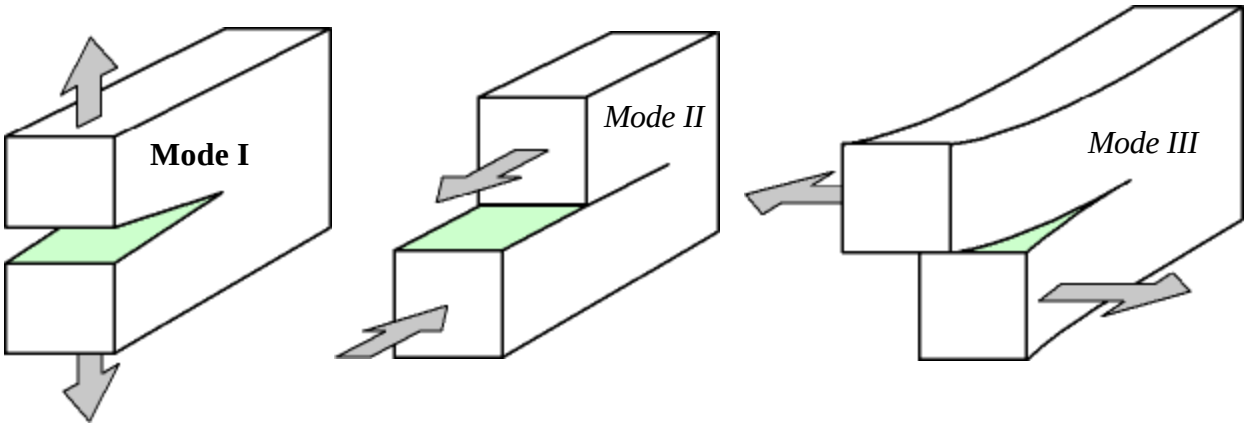

Fig. 5.1. Different modes of fracture – mode I , II and III

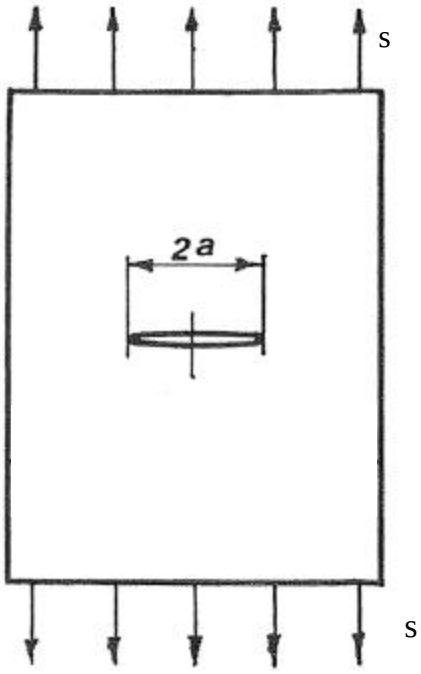

Fig. 5.2 An infinite plate with a crack loaded with far-field tensile stress

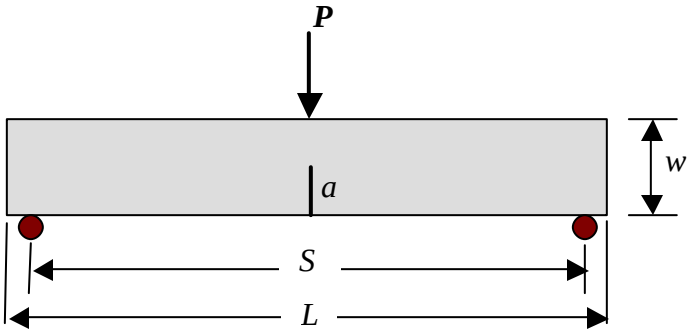

Fig. 5.3 Single edge notched beam configuration (SENB)

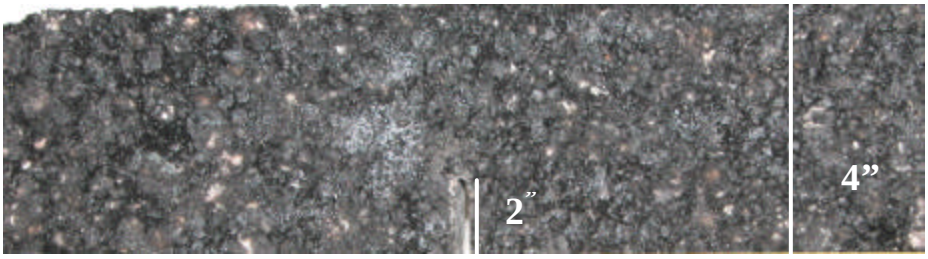

(a) Large beams

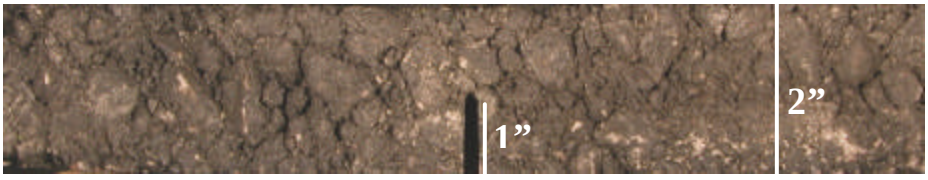

(b) Small beams

Fig. 5.4 Specimen beam geometries

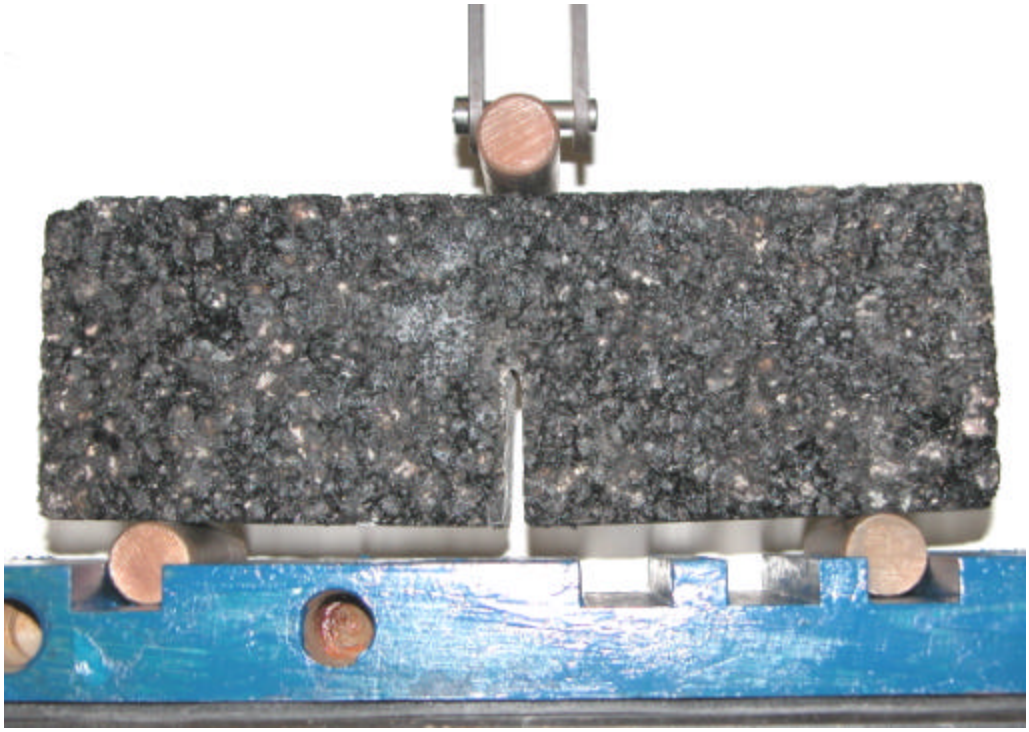

Fig. 5.5 Setup for testing quasi-static fracture behavior

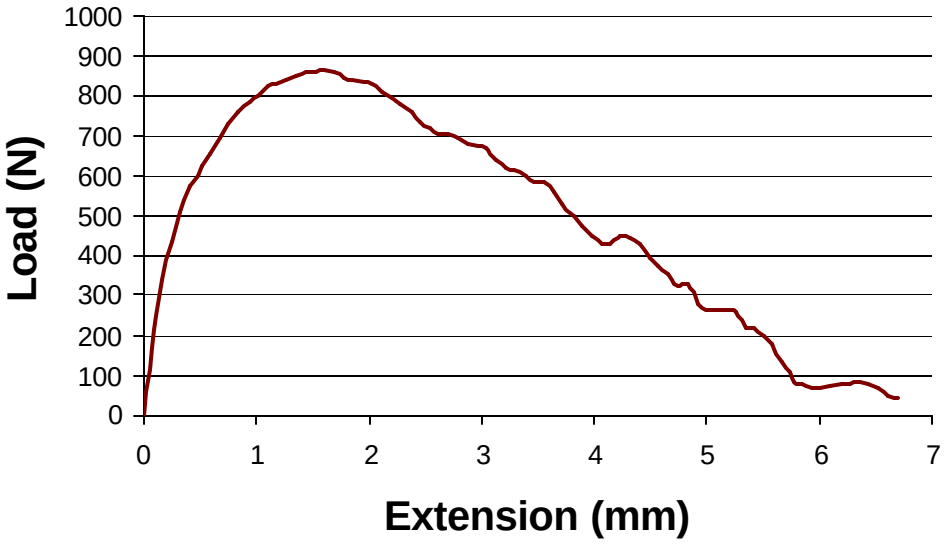

Fig. 5.6 Typical load-deformation plot for quasi-static fracture toughness tests

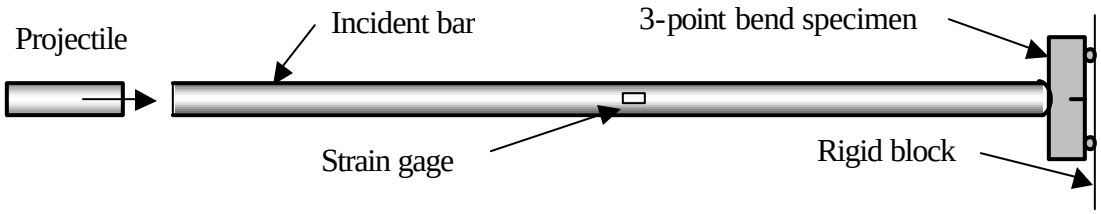

Fig. 5.7 Schematic of modified Hopkinson pressure bar setup

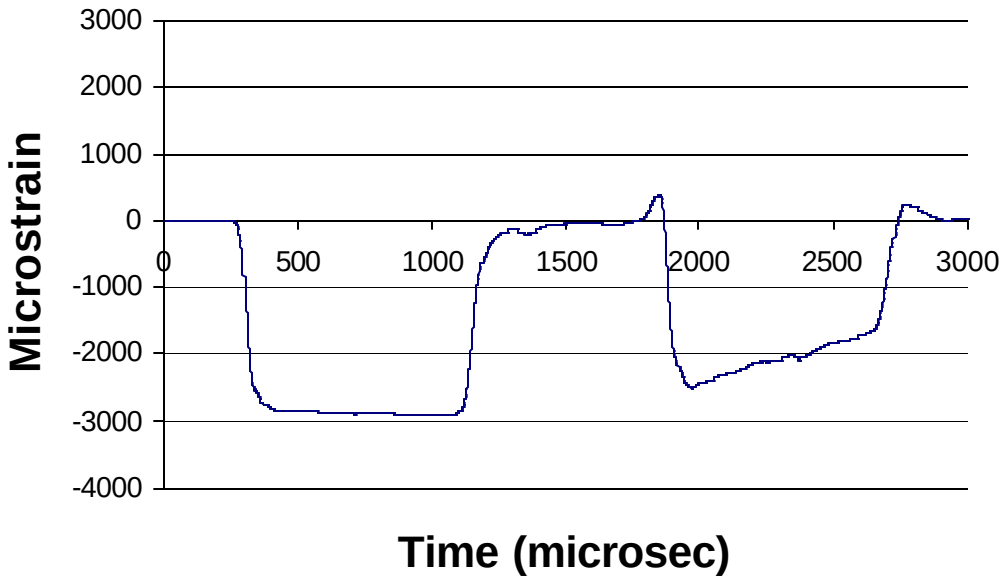

Fig. 5.8 Typical strain-time history of dynamically loaded fracture specimens

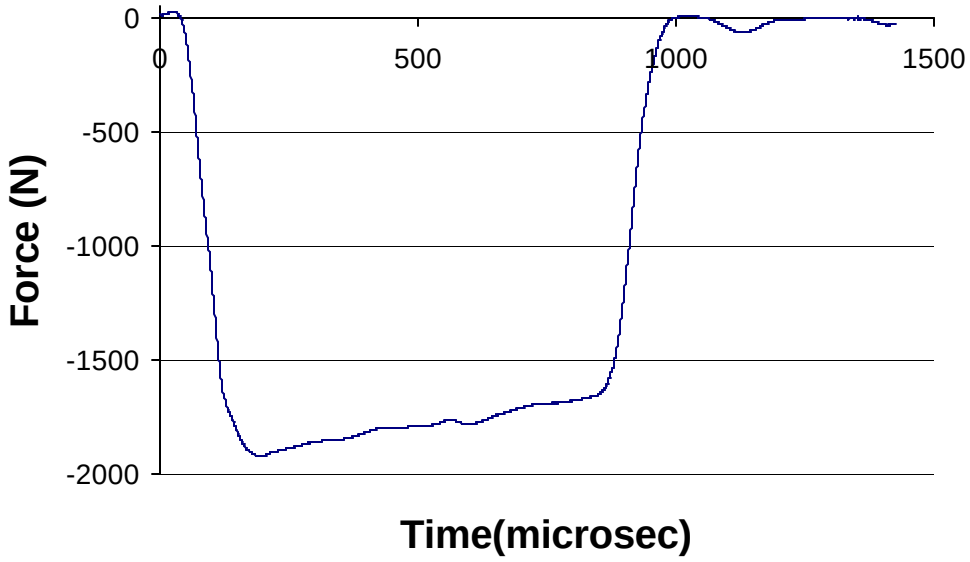

Fig. 5.9 Force-time history of dynamically loaded fracture specimens

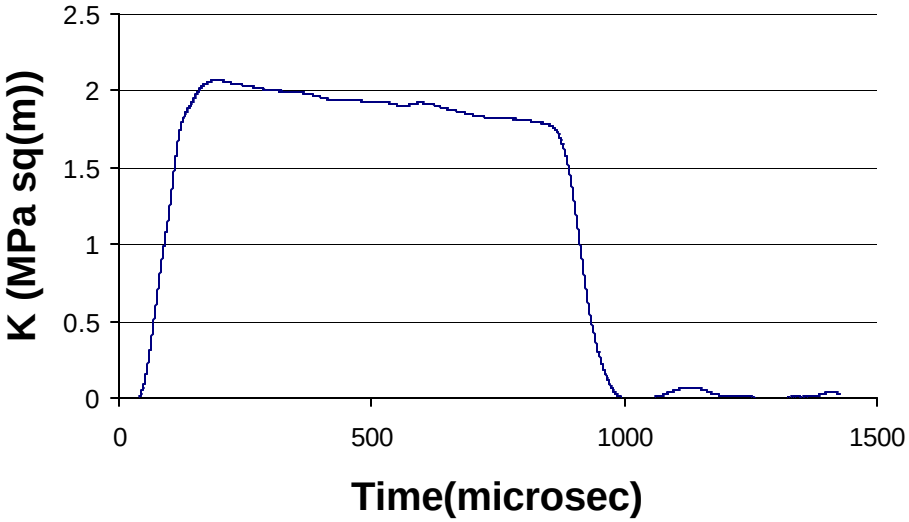

Fig. 5.10 Typical stress intensity factor time profile

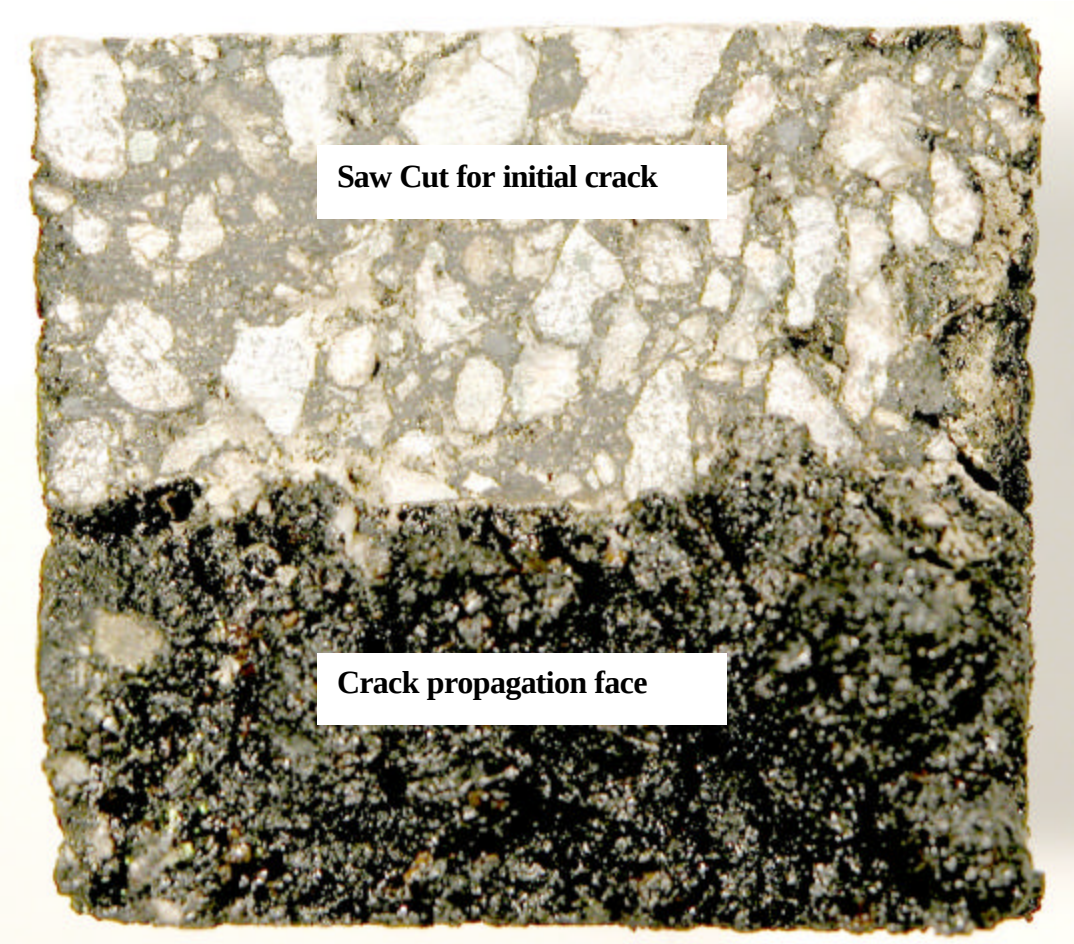

Fig. 5.11 Crack face and fracture surface obtained from quasi-static fracture test.

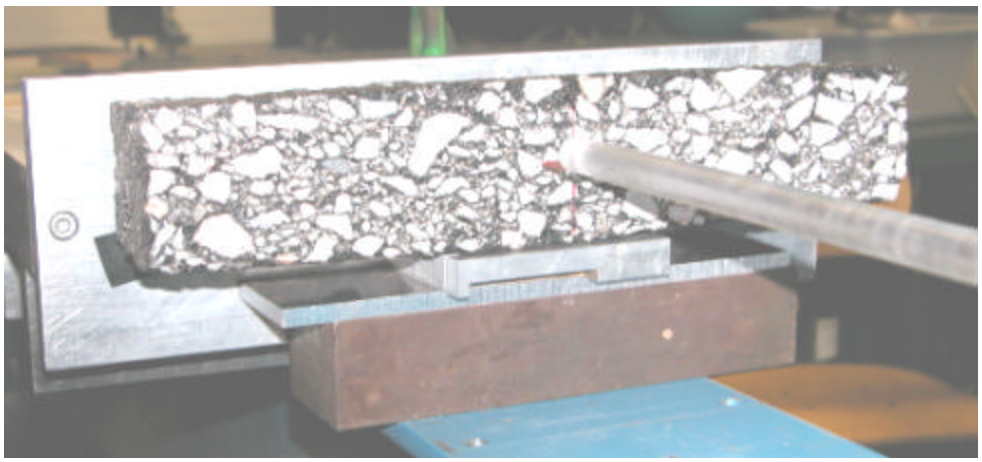

Fig. 5.12 Dynamic fracture setup with failed specimen due to impact loading of incident bar.

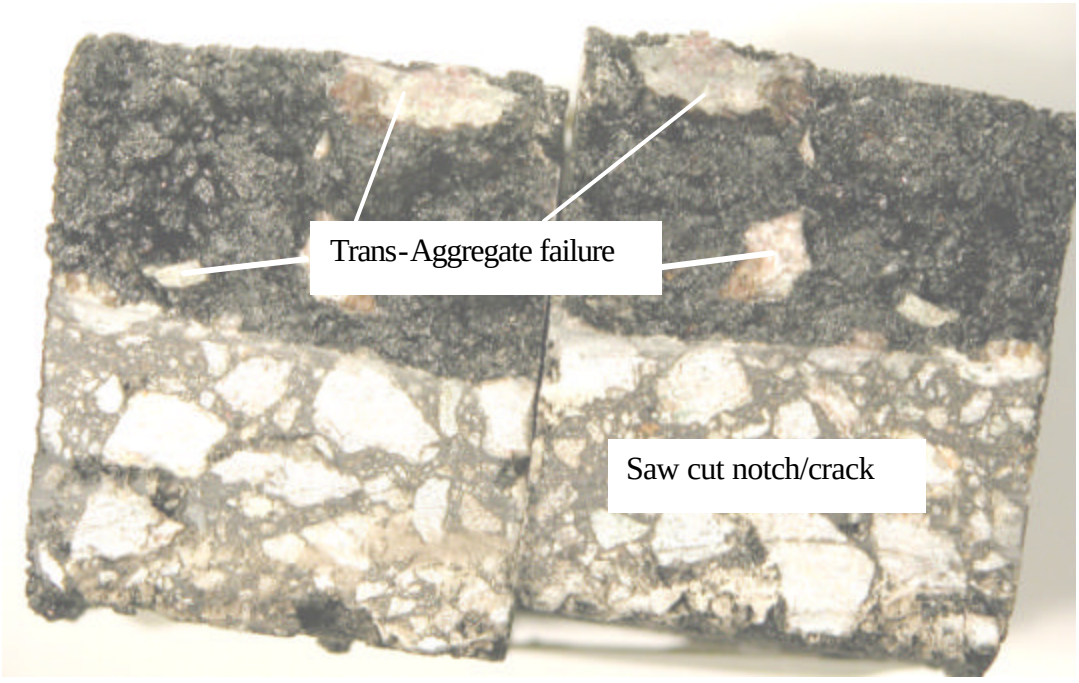

Fig. 5.13 Crack face and fracture surfaces obtained from dynamic fracture testing.
(Fractured aggregates marked)

6. MICROMECHANICAL DAMAGE-COUPLED VISOCELASTIC MODEL FOR ASPHALT MATERIALS

6.1 Introduction

This section outlines our numerical modeling work, which has included extensions of our previous micromechanical finite element technique. Numerical modeling of cemented particulate materials has generally used both finite (FEM) and discrete (DEM) element methods. In regard to finite element modeling, Sepehr et al. (1994) used an idealized finite element microstructural model to analyze the behavior of an asphalt pavement layer. Soares et al. (2003) used cohesive zone elements to develop a micromechanical fracture model of asphalt materials. A particular finite element approach to simulate particulate materials has used an *equivalent lattice network system* to represent the interparticle load transfer behavior. Guddati et al. (2002) recently presented a random truss lattice model to simulate microdamage in asphalt concrete and demonstrated some interesting failure patterns in an indirect tension test geometry. Sadd et al. (2004a,b) employed a micro-frame network model to investigate the damage behavior of asphalt materials, this model used a special purpose finite element that incorporates the mechanical load-carrying response between neighboring particles. Bahia et al. (1999) have also used finite elements to model the aggregate-mastic response of asphalt materials.

Damage mechanics provides a viable framework for the description of asphalt stiffness degradation, microcrack initiation, growth and coalescence, and damage-induced anisotropy. Continuum damage mechanics is based on the thermodynamics of irreversible processes to characterize elastic-coupled damage behaviors. Chaboche (1988), and Simo and Ju (1987) developed strain- and stress-based anisotropic continuum damage models, while Kachanov (1987) proposed a microcrack-related continuum brittle damage model for brittle solids. For viscoelastic materials, a three-dimensional continnum damage model was proposed by Simo (1987). Schapery (1984) developed detailed viscoelastic damage models based on nonequilibrium thermodynamics, viscoelastic fracture mechanics and elastic-viscoelastic correspondence principles, and a later study (1991) incorporated a work potential theory. Park and Schapery (1996) proposed an explicit viscoelastic damage model for particulate composites, and Park, et al. (1996) applied this model to uniaxial behavior of asphalt concrete. Recently, Schapery (1999) developed constitutive equations that account for effects of viscoelastic, viscoplastic, growing damage and aging. Some recent studies were conducted on damage constitutive modeling of viscoelastic composite materials, such as Canga et al. (2001), Kaliske et

al. (2001), Haj-Ali and Muliana (2003), and Kumar and Talreja (2001). Wu and Harvey (2003) recently applied a 3D continuum damage mechanics method to model the cracking behavior of asphalt concrete.

Our current work (Dai and Sadd, 2004) presents a micromechanical modeling scheme for the damage-coupled viscoelastic behavior of asphalt materials by using finite element methods. The model incorporates the user-defined material subroutine with continuum elements for the effective asphalt mastic and rigid body defined with rigid elements for each aggregate. A unified approach for the rate-independent failure and rate-dependent damage behavior has been developed using Schapery's nonlinear viscoelastic model. Properties of the continuum elements are specified through a user material subroutine within the ABAQUS code and this allows damage-coupled viscoelastic constitutive behavior of the mastic cement to be incorporated. We first outline the finite element incremental algorithm with recursive relationships, and this algorithm is later used in the 3D viscoelastic damage modeling of the asphalt mastic in the proposed microstructure model. Next, we present the basic concepts of our microstructural modeling of heterogeneous asphalt materials. The cyclic loading response of viscoelastic asphalt materials with/without rate-independent damage behavior is then compared, and this is followed by an investigation of the effect of loading rate on the viscoelastic damage behavior of an asphalt numerical sample. Finally, we compare model uniaxial tensile simulation under different loading rates with test data from the work by Lee and Kim (1998).

6.2 Damage-Coupled Viscoelastic Model

6.2.1 One-Dimensional Linear Viscoelastic Model

A generalized Maxwell model is commonly used to simulate the constitutive behavior of linear solid viscoelastic material. This model consists of an elastic spring with constant E_∞ in parallel with M Maxwell elements. The stress-strain relationship for this model can be expressed as a hereditary integral

$$s = E_\infty e + \int_0^t E_t \frac{de(t)}{dt} dt \tag{6.1}$$

where E_t is expressed with a Prony series

$$E_t = \sum_{m=1}^{M} E_m e^{-\frac{(t-t)}{r_m}}, \text{ and } r_m = \frac{h_m}{E_m} \tag{6.2}$$

In these equations, E_∞ is the relaxed elastic modulus, E_t is the transient modulus as a function of the time, E_m, h_m and r_m are the spring constant, dashpot viscosity and relaxation time respectively for the m^{th} Maxwell element.

The reduced time (effective time) is defined by using time-temperature superposition principle as

$$x(t) = \int_0^t \frac{1}{a_T} dt \tag{6.3}$$

where the term $a_T = a_T(T(t))$ is a temperature-dependent time-scale shift factor.

A displacement based incremental finite element modeling scheme with constant strain rate over each increment has been developed. An incremental numerical algorithm for the linear viscoelastic integral has been used from the work of Zocher (1997). This algorithm was developed in closed form and results in a recursive relationship. This method allows the incremental formulation of the current stress state from recursive variables stored in the previous step with current variables, time and strain increments.

Assume the stress is known at the reduced time x_{n-1}, and the current stress at reduced time x_n, according to (6.1), is given by

$$s(x_n) = E_\infty e(x_n) + \int_0^x E_t(x_n - x') \frac{de(x')}{dx'} dx' \tag{6.4}$$

Its incremental form can be written in two parts,

$$\Delta s = E' \cdot \Delta e + \Delta s^R \tag{6.5}$$

The first part includes the integration from the previous step x_{n-1} to the current step x_n. The reduced time increment is defined as $\Delta x = x_n - x_{n-1}$. This formulation assumes the incremental strain $\Delta e = e_n - e_{n-1}$ is known, and the strain changes with a constant strain rate R_e during each interval $x_{n-1} \le x' \le x_n$. So the incremental modulus E' and strain rate R_e can be expressed by

$$E' = E_\infty + \sum_{m=1}^{M} \frac{E_m r_m}{\Delta x} \left(1 - e^{-\frac{\Delta x}{r_m}} \right), \text{ and } R_e = \frac{\Delta e}{\Delta x} \tag{6.6}$$

Note that the incremental stiffness E' is not dependent on the time if Δx remains constant. The second part is formulated with integration from 0 to the previous step x_{n-1}, and this leads to a recursive relation with the history variables S_m.

$$\Delta s^R = \sum_{m=1}^{M} -\left(1 - e^{-\frac{\Delta x}{r_m}}\right) S_m(x_n), \text{ and } S_m(x_n) = E_m R_e r_m \left(1 - e^{-\frac{\Delta x}{r_m}}\right) + S_m(x_{n-1}) e^{-\frac{\Delta x}{r_m}} \quad (6.7)$$

6.2.2 One-Dimensional Damage-Coupled Viscoelastic Model

Rate-independent failure processes are characterized by the fact that damage growth is the only dissipative mechanism and that the current state does not depend on the rate (Marigo (1985)). The rate-independent damage variable is defined as a function of maximum equivalent strain (Simo (1987)). While rate-dependent damage is caused by the loading rate, and the damage variable is based on the equivalent strain rate. A unified approach is presented for both failure mechanisms by using Schapery nonlinear viscoelastic model.

The original Schapery nonlinear viscoelastic model was given by Schapery (1969)

$$s(x) = h_e E_\infty e(x) + \int_0^x h_1 E_t(x - x') \frac{d(h_2 e(x'))}{dx'} dx' \quad (6.8)$$

This model incorporates three different nonlinear parameters: h_e is the nonlinear factor of the relaxed elastic modulus E_∞, h_1 measures the nonlinearity effect in the transient modulus E_t, and h_2 accounts for the loading rate effect.

Following form (6.8), a unified damage-coupled viscoelastic model for both failure mechanisms is proposed by replacing three nonlinear parameters with damage variables which would be expressed with damage evolution functions.

$$s(x) = h_e(e_{\max}) E_\infty e(x) + \int_0^x h_1(e_{\max}) E_t(x - x') \frac{d(h_2(\dot{e}) e(x'))}{dx'} dx' \quad (6.9)$$

where h_e and h_1 are the elastic and viscoelastic damage variables for the rate-independent failure behavior, h_2 is the rate-dependent damage variable dependent on the strain rate $\dot{e}$. The rate-independent variables h_e and h_1 are functions of maximum strain $e_{\max}$, which is defined as the maximum value over the past history up to the current time x,

$$e_{\max} = \max(e(x')),\ x' \in (0, x) \quad (6.10)$$

The elastic damage variable $h_e = 1 - \Omega$ measures the relaxed elastic stiffness reduction, and can be described by using our inelastic damage evolution law in Sadd et al. (2004a,b)

$$h_e(e_{\max}) = e^{-b\frac{e_{\max}}{e_0}} \tag{6.11}$$

where the material parameters e_0 and b are related to the softening strain and damage evolution rate respectively.

The viscoelastic variable h_1 measures the damage effect in the transient modulus, and is chosen with the following exponential form by Simo (1987),

$$h_1(e_{\max}) = b + (1-b)\frac{1-e^{-\frac{e_{\max}}{e_0}}}{e_{\max}/e_0},\ b \in [0,1] \tag{6.12}$$

The variable h_1 will reduce from 1 to b as the maximum strain $e_{\max}$ increases, and e_0 is also the softening stain.

The rate-dependent damage variable h_2 is proposed as

$$h_2 = \left(1 + \left\langle \frac{\dot{e}}{\dot{e}_C} - 1 \right\rangle\right)^{-a} \Rightarrow h_2 = \begin{cases} \left(\dfrac{\dot{e}}{\dot{e}_C}\right)^{-a}, & \text{if } \dot{e} \geq \dot{e}_C \\ 1, & \text{if } \dot{e} < \dot{e}_C \end{cases} \tag{6.13}$$

where $\dot{e}_C$ is the threshold strain rate that determines the start of the rate-dependent damage, and $a \geq 0$ is related to the rate-dependent damage evolution rate. When the parameter a = 0 or loading rate $\dot{e} < \dot{e}_C$, h_2 = 1 and this model only has rate-independent damage behavior.

The incremental formulation of the 1D damage-coupled viscoelastic behavior can be established by using a similar procedure as used in the previous section. According to relation (6.9), the current stress at reduced time x_n is given by

$$s(x_n) = h_e(e_{\max})E_\infty e(x_n) + \int_0^{x_n} h_1(e_{\max})E_t(x_n - x')\frac{dh_2(\dot{e})e(x')}{dx'}dx' \tag{6.14}$$

and its incremental form can also be formulated into two parts

$$\Delta s = E' \cdot \Delta e + \Delta s^R \tag{6.15}$$

Assuming again that the strain changes with constant rate R_e during each interval $x_{n-1} \leq x' \leq x_n$, the first term in equation (6.15) gives the incremental modulus E' as

$$E' = h_e(e_{\max})E_\infty + h_1(e_{\max})h_2(R_e)\sum_{m=1}^{N}\frac{E_m r_m}{\Delta x}\left(1-e^{-\frac{\Delta x}{r_m}}\right)$$
$$\text{where } R_e = \frac{\Delta e}{\Delta x} \text{ and } h_2(R_e) = \begin{cases}\left(\frac{R_e}{\dot{e}_C}\right)^{-a}, & \text{if } R_e \geq \dot{e}_C \\ 1, & \text{if } R_e < \dot{e}_C\end{cases} \tag{6.16}$$

This incremental modulus E' includes both rate-independent and rate-dependent damage variables. The second term of (6.15) also leads to a recursive relation with the history variables S_m, and S_m includes the viscoelastic damage variable h_1 and rate-dependent damage variable h_2,

$$\Delta s^R = \sum_{m=1}^{N} -\left(1-e^{-\frac{\Delta x}{r_m}}\right)S_m(x_n),$$
$$\text{and } S_m(x_n) = E_m h_1(e_{\max})h_2(R_e)R_e r_m\left(1-e^{-\frac{\Delta x}{r_m}}\right) + S_m(x_{n-1})e^{-\frac{\Delta x}{r_m}} \tag{6.17}$$

This model includes two damage mechanisms when the strain rate $\dot{e}$ is equal or larger than the threshold strain rate $\dot{e}_C$, and has only rate-independent damage behavior if the strain rate is less than this threshold value.

6.2.3 Three-Dimensional Damage-Coupled Viscoelastic Model

The numerical formulations for 1D damage-coupled viscoelastic behavior are generalized in the multiaxial (3D) constitutive relations for isotropic matrix medium. As employed by Simo (1987), and Haj-Ali and Muliana (2003), uncoupled volumetric and deviatoric stress-strain relations are assumed. The formulation also assumes the incremental strain tensor is known and the strains change linearly during each interval $x_{n-1} \leq x' \leq x_n$.

From the elasticity theory, the stress and strain tensors can be decomposed into the sum of volumetric and devitoric parts

$$s_{ij} = 1/3 s_{kk} d_{ij} + \hat{s}_{ij},\ e_{ij} = 1/3 e_{kk} d_{ij} + \hat{e}_{ij} \tag{6.18}$$

The elastic stress-strain relations for the volumetric and deviatoric behavior are expressed by

$$s_{kk} = 3Ke_{kk},\ \hat{s}_{ij} = 2G\hat{e}_{ij} \tag{6.19}$$

where $K = \frac{E}{3(1-2u)}$ and $G = \frac{E}{2(1+u)}$ are the elastic bulk and shear modulus. The terms K_∞ and G_∞ are the relaxed bulk and shear modulus, and K_m and G_m are the bulk and shear constants for the spring in the m^{th} Maxwell element.

By applying the previous 1D damage-coupled viscoelastic model, the volumetric constitutive relationship is expressed with the volumetric stress s_{kk} and strain e_{kk} in the general form

$$s_{kk}(x) = 3K_\infty h_e\left(e_{\max}^{kk}\right)e_{kk}(x) + \int_0^x 3K_t(x-x')h_1\left(e_{\max}^{kk}\right)\frac{dh_2(\dot{e}_{kk})e_{kk}(x')}{dx'}dx' \tag{6.20}$$

where $K_t(x-x') = \sum_{m=1}^{M} K_m e^{-\frac{(x-x')}{r_m}}$ is the transient bulk modulus, $e_{\max}^{kk}$ is the maximum volumetric strain over the past history, and $\dot{e}_{kk}$ is the volumetric strain rate. It is assumed that tension and compression damage behaviors are independent, so two different history variables $e_{\max}^{kk}$ are used for the tension and compression volumetric behaviors.

Following our previous formulation procedure, the incremental formulation of the volumetric behavior is obtained with constant volumetric strain rate $R_{kk} = \frac{\Delta e_{kk}}{\Delta x}$,

$$\begin{aligned}\Delta s_{kk} &= 3\left[K_\infty h_e\left(e_{\max}^{kk}\right) + \sum_{m=1}^{N} h_1\left(e_{\max}^{kk}\right)h_2(R_{kk})\frac{K_m r_m}{\Delta x}\left(1-e^{-\frac{\Delta x}{r_m}}\right)\right]\Delta e_{kk} + \Delta s_{kk}^{R} \\ \text{where } h_2(R_{kk}) &= \begin{cases}\left(\frac{R_{kk}}{\dot{e}_C}\right)^{-a}, & \text{if } R_{kk} \geq \dot{e}_C \\ 1, & \text{if } R_{kk} < \dot{e}_C\end{cases}\end{aligned} \tag{6.21}$$

and the residual part Δs_{kk}^{R} can be expressed in this recursive relation with the history variable S_m.

$$\begin{aligned}\Delta s_{kk}^{R} &= \sum_{m=1}^{M} -\left(1-e^{-\frac{\Delta x}{r_m}}\right)S_m(x_n) \\ \text{and } S_m(x_n) &= 3K_m h_1\left(e_{\max}^{kk}\right)h_2(R_{kk})R_{kk}\, r_m\left(1-e^{-\frac{\Delta x}{r_m}}\right) + S_m(x_{n-1})e^{-\frac{\Delta x}{r_m}}\end{aligned} \tag{6.22}$$

For the deviatoric behavior, the constitutive relationship is written with deviatoric stress $\hat{s}_{ij}$ and strain $\hat{e}_{ij}$,

$$\hat{s}_{ij}(x) = 2G_\infty h_e\left(e_{\max}^{e}\right)\hat{e}_{ij}(x) + \int_0^x 2G_t(x-x')h_1\left(e_{\max}^{e}\right)\frac{dh_2(\dot{e}_e)\hat{e}_{ij}(x')}{dx'}dx' \tag{6.23}$$

where $G_t(x-x') = \sum_{m=1}^{N} G_m e^{-\frac{(x-x')}{r_m}}$ is the transient shear modulus, $e^e_{\max}$ is the maximum equivalent strain, and the equivalent strain e_e and strain rate $\dot{e}_e$ are defined as

$$e_e = \sqrt{\frac{3}{2}\hat{e}_{ij}\hat{e}_{ij}} \text{ and } \dot{e}_e = \sqrt{\frac{3}{2}\dot{\hat{e}}_{ij}\dot{\hat{e}}_{ij}} \tag{6.24}$$

The formulation of the deviatoric behavior is obtained with constant deviatoric strain rate tensor $\hat{R}_{ij} = \frac{\Delta\hat{e}_{ij}}{\Delta x}$,

$$\begin{aligned} \Delta\hat{s}_{ij} &= 2\left[G_\infty h_e(e^e_{\max}) + \sum_{m=1}^{N} h_1(e^e_{\max}) h_2(R_e) \frac{G_m r_m}{\Delta x}\left(1 - e^{-\frac{\Delta x}{r_m}}\right)\right]\Delta\hat{e}_{ij} + \Delta\hat{s}^R_{ij} \\ \text{where } R_e &= \sqrt{\frac{3}{2}\hat{R}_{ij}\hat{R}_{ij}} \text{ and } h_2(R_e) = \begin{cases} \left(\frac{R_e}{\dot{e}_C}\right)^{-a}, & \text{if } R_e \geq \dot{e}_C \\ 1, & \text{if } R_e < \dot{e}_C \end{cases} \end{aligned} \tag{6.25}$$

and the residual part $\Delta\hat{s}^R_{ij}$ can be expressed in this recursive relation

$$\begin{aligned} \Delta\hat{s}^R_{ij} &= \sum_{m=1}^{N} -\left(1 - e^{-\frac{\Delta x}{r_m}}\right) S_m(x_n) \\ \text{and } S_m(x_n) &= 2G_m h_1(e^e_{\max}) h_2(R_e)\hat{R}_{ij} r_m\left(1 - e^{-\frac{\Delta x}{r_m}}\right) + S_m(x_{n-1}) e^{-\frac{\Delta x}{r_m}} \end{aligned} \tag{6.26}$$

The incremental normal stresses can be then formulated by combining the volumetric and deviatoric behavior, for example,

$$\begin{aligned} \Delta s_{xx} &= 1/3\Delta s_{kk} + \Delta\hat{s}_{xx} \\ &= \left[K_\infty h_e(e^{kk}_{\max}) + \sum_{m=1}^{N} h_1(e^{kk}_{\max}) h_2(R_{kk}) \frac{K_m r_m}{\Delta x}\left(1 - e^{-\frac{\Delta x}{r_m}}\right)\right]\Delta e_{kk} \\ &+ 2\left[G_\infty h_e(e^e_{\max}) + \sum_{m=1}^{N} h_1(e^e_{\max}) h_2(R_e) \frac{G_m r_m}{\Delta x}\left(1 - e^{-\frac{\Delta x}{r_m}}\right)\right]\Delta\hat{e}_{xx} + 1/3\Delta s^R_{kk} + \Delta\hat{s}^R_{xx} \end{aligned} \tag{6.27}$$

where Δe_{kk} and Δs_{kk} are the incremental volumetric strain and stress, $\Delta\hat{e}_{xx}$ and $\Delta\hat{s}_{xx}$ are the incremental deviatoric strain and stress components, and Δs^R_{kk} and $\Delta\hat{s}^R_{xx}$ are the recursive part of the volumetric and deviatoric behavior given in Eqns. (6.22) and (6.26). Incremental stresses Δs_{yy} and Δs_{zz} are determined in the same manner.

The incremental shear stress can be formulated by using the deviatoric behavior. For example,

$$\begin{aligned}\Delta s_{xy} &= \Delta \hat{s}_{xy} \\ &= 2\left[G_\infty h_e\left(e^{e}_{\max}\right) + \sum_{m=1}^{N} h_1\left(e^{e}_{\max}\right) h_2\left(R_e\right) \frac{G_m r_m}{\Delta x}\left(1 - e^{-\frac{\Delta x}{r_m}}\right)\right] \Delta \hat{e}_{xy} + \Delta \hat{s}^{R}_{xy}\end{aligned} \tag{6.28}$$

where $\Delta \hat{e}_{xy}$ and $\Delta \hat{s}_{xy}$ are the incremental *shear* deviatoric strain and stress components, and the recursive term $\Delta \hat{s}^{R}_{xy}$ is also given in Eqn. (6.26).

Once the incremental stress components were developed, the incremental stiffness (Jacobin) matrix can be constructed with these terms:

$$\begin{aligned}\frac{\partial \Delta s_{xx}}{\partial \Delta e_{xx}} &= \left[K_\infty h_e\left(e^{e}_{\max}\right) + \sum_{m=1}^{N} h_1\left(e^{e}_{\max}\right) h_2\left(R_{kk}\right) \frac{K_m r_m}{\Delta x}\left(1 - e^{-\frac{\Delta x}{r_m}}\right)\right] + \frac{4}{3}\left[G_\infty h_e\left(e^{e}_{\max}\right) + \sum_{m=1}^{N} h_1\left(e^{e}_{\max}\right) h_2\left(R_e\right) \frac{G_m r_m}{\Delta x}\left(1 - e^{-\frac{\Delta x}{r_m}}\right)\right] \\ &= K_{d1} \\ \frac{\partial \Delta s_{xx}}{\partial \Delta e_{yy}} &= \left[K_\infty h_e\left(e^{e}_{\max}\right) + \sum_{m=1}^{N} h_1\left(e^{e}_{\max}\right) h_2\left(R_{kk}\right) \frac{K_m r_m}{\Delta x}\left(1 - e^{-\frac{\Delta x}{r_m}}\right)\right] - \frac{2}{3}\left[G_\infty h_e\left(e^{e}_{\max}\right) + \sum_{m=1}^{N} h_1\left(e^{e}_{\max}\right) h_2\left(R_e\right) \frac{G_m r_m}{\Delta x}\left(1 - e^{-\frac{\Delta x}{r_m}}\right)\right] \\ &= K_{d2} \\ \frac{\partial \Delta s_{xy}}{\partial \Delta e_{xy}} &= 2\left[G_\infty h_e\left(e^{e}_{\max}\right) + \sum_{m=1}^{N} h_1\left(e^{e}_{\max}\right) h_2\left(R_e\right) \frac{G_m r_m}{\Delta x}\left(1 - e^{-\frac{\Delta x}{r_m}}\right)\right] = K_{d3}\end{aligned} \tag{6.29}$$

With these terms, the incremental 3D damage-coupled viscoelastic behavior can be formulated as

$$\begin{bmatrix}\Delta s_{xx} \\ \Delta s_{yy} \\ \Delta s_{zz} \\ \Delta s_{xy} \\ \Delta s_{yz} \\ \Delta s_{xz}\end{bmatrix} = \begin{bmatrix}K_{d1} & K_{d2} & K_{d2} & 0 & 0 & 0 \\ \cdot & K_{d1} & K_{d2} & 0 & 0 & 0 \\ \cdot & \cdot & K_{d1} & 0 & 0 & 0 \\ \cdot & \cdot & \cdot & K_{d3} & 0 & 0 \\ \cdot & \cdot & \cdot & \cdot & K_{d3} & 0 \\ \cdot & \cdot & \cdot & \cdot & \cdot & K_{d3}\end{bmatrix} \begin{bmatrix}\Delta e_{xx} \\ \Delta e_{yy} \\ \Delta e_{zz} \\ \Delta e_{xy} \\ \Delta e_{yz} \\ \Delta e_{xz}\end{bmatrix} + \begin{bmatrix}\Delta s^{R}_{kk} + \Delta \hat{s}^{R}_{xx} \\ \Delta s^{R}_{kk} + \Delta \hat{s}^{R}_{yy} \\ \Delta s^{R}_{kk} + \Delta \hat{s}^{R}_{zz} \\ \Delta \hat{s}^{R}_{xy} \\ \Delta \hat{s}^{R}_{yz} \\ \Delta \hat{s}^{R}_{zx}\end{bmatrix} \tag{6.30}$$

This damage-coupled viscoelastic model can then be defined in ABAQUS user material subroutine, and this subroutine has been combined with ABAQUS elements to implement a displacement-based nonlinear finite element analysis.

6.3 Micromechanical Modeling

Because of the heterogeneous nature of asphalt, its load carrying behavior is strongly related to the local load transfer through the effective mastic zone between aggregate particles, and this is taken as the microstructural response. The aggregate material is normally much stiffer than the mastic, and thus aggregates are taken as rigid particles. On the other hand, the mastic

cement is a compliant material with elastic, inelastic, and time-dependent behaviors. Additionally, mastic behavior can also include hardening, debonding and microcracking, and these lead to many complicated failure mechanisms. In general, asphalt concrete contains aggregate of very irregular geometry as shown in Fig. 6.1(a). Our approach is to allow variable size and shape using an elliptical aggregate model as represented in Fig. 6.1(b). The finite element model shown in Fig. 6.1(c) uses a rectangular strip to simulate the effective asphalt mastic zone, and incorporates the ABAQUS user material subroutine with continuum elements to model the effective asphalt mastic behavior.

As shown in Fig. 6.2, the general modeling scheme employed four-node quadrilateral elements to mesh the effective cement material, and a rigid body defined with two-node rigid elements sharing the particle center to model each aggregate. The particle center is referred to as the master node of the aggregate rigid body, and thus each rigid body element would have identical translation and rotation as the aggregate. The rigid elements act to link the mastic deformation with the aggregate rigid body motion thereby establishing the micromechanical deformation behavior. Properties of the quadrilateral elements are specified through a user defined material subroutine within the ABAQUS code and this allows incorporation of our developed damage-coupled viscoelastic mastic cement models.

6.4 Numerical Simulation

6.4.1 Cyclic Loading Responses

A two-dimensional indirect tension testing sample has been generated with MATLAB and its mesh figure was modeled by using ABAQUS elements as shown in Fig. 6.3. This particular model has 65 particles (in four particle size groupings), 195 effective mastic zones, 7.6% porosity and an approximate overall diameter of 101mm (4in). This microgeometry results in a total of 780 deforming mastic elements and 1170 rigid aggregate elements with connectivity as shown. The mastic elements had 3-parameter viscoelastic constitutive properties with relaxed elastic moduli $E_¥$ = 412.8 MPa and one Maxwell element of spring constant E_1 = 1232 Mpa and relaxation time r_1 = 6.5 s. These constitutive properties were selected from asphalt concrete characterization testing by Gibson [30]. It was assumed that Poisson's ratio u didn't change with time and was given as 0.3. Model rate-independent damage parameters were chosen as b=1, b = 0.3, and softening strain e_0= 0.2. The rate-dependent damage parameter a was

taken as zero, and thus this study compares the rate-independent damage with linear viscoelastic behavior.

For the following cyclic loading simulations, both displacement- and force-controlled boundary conditions were used on the numerical sample. For the displacement-controlled boundary conditions, both horizontal and vertical displacements of the bottom pair of aggregates are constrained, and the top particle pair accept the applied vertical displacement loading. While in the force-control, the vertical force is imposed to the top particle pair, and the displacements of the bottom pair of aggregates are again constrained.

Linear and damage-coupled viscoelastic simulations were conducted and compared for both displacement- and force-controlled boundary conditions. Fig. 6.4(a, b) shows the sample responses under unreversed saw-toothed loading. In these figures, linear viscoelastic behavior is indicated with the solid line, and damage-coupled viscoleastic behavior is shown with dot/dash line. Viscoelastic behavior is demonstrated by the decreasing relaxation force and increasing creep displacement with the unreversed cyclic loading time. The results also show that viscoelastic damage behavior reduces the sample's loading support ability for the displacement-controlled boundary conditions, and increases the sample creep displacement for the force loading. Fig. 6.5(a, b) shows the sample responses under reversed saw-toothed loading. Linear and damage-coupled viscoelastic behaviors are again compared for force- and displacement-controlled boundary conditions. These figures also show a sample stiffness decrease with increase of loading for the rate-independent damage behavior. Both linear and damage-coupled viscoelastic simulations reach steady-state response after very few reversed cycles.

Numerical simulations were also conducted with an incrementally increasing reversed cyclic loading as shown in Fig. 6.6. Figure 6.6(a) shows the linear viscoelastic responses of the numerical sample under the displacement and force loading. The maximum points in each loop are approximately located along a straight line in these two figures. Figure 6.6(b) gives the damage-coupled viscoelastic responses. Since the rate-independent damage variables in our model are all defined as exponential functions, the maximum points are distributed along an exponential curve by increasing creep displacement and reducing relaxation force. These damage-coupled cyclic responses illustrate that rate-independent damage increases with the maximum deformation. This occurs since the rate-independent damage parameters are the function of maximum strain. These results also demonstrate the Mullins effect (Mullins [31]). For a cyclic response, this effect results in a progressive reduction of the storage moduli with

increasing maximum strain amplitude. Almost all of the loss in stiffness takes place during the first cyclic deformation, and the subsequent cyclic behavior is expected to be hardened. Thus the steady-state response is obtained after very few cycles with the same loading amplitude.

6.4.2 Loading Rate Effect

In the previous section, rate-independent damage behavior of viscoelastic asphalt materials under cyclic loading was investigated. We now wish to investigate rate-dependent damage behavior where the strain rate $\dot{e}$ is larger than the threshold strain rate $\dot{e}_C$ and the parameter a has a positive value. For the following loading rate effect study, indirect tension simulations were conducted on the same numerical sample (shown in Fig. 6.3) with the displacement-controlled boundary conditions. These simulations used the same 3-parameter viscoelastic constitutive properties as before, and the identical rate-independent damage parameters were chosen as b =1, $b = 0.5$, and softening strain e_0 = 0.1.

Effects of the two model parameters $\dot{e}_C$ and a of rate-dependent damage variable h_2 are studied in Fig. 6.7. The loading displacement increases linearly from zero to 6 mm with a loading rate 0.6 mm/s. Figure 6.7(a) shows the simulation results for three different threshold strain rates $\dot{e}_C$ with constant a. These results indicate that more rate-dependent damage is generated as the threshold strain rate decreases. Figure 6.7(b) shows simulation results for the cases of $a = 0.1$, 0.3 and 0.5 with constant threshold strain rate. Note that the sample has more rate-dependent damage behavior for the larger a value.

Results of loading rate effects on asphalt viscoelastic damage behavior are shown in Fig. 6.8. For these indirect tension simulations, rate-dependent damage parameters were chosen as $\dot{e}_C = 0.001$ and $a = 0.1$. Figure 6.8(a) shows the simulation results under the monotonic linear displacement loading to the same compression displacement 5 mm at loading rates of 5, 1, 0.5 and 0.25 mm/s. Solid lines indicate the linear viscoelastic behavior, dashed lines indicate the damage-coupled viscoelastic behavior. Higher loading rates generate the larger sample reaction forces since it has less relaxation time. Comparing the linear and damage-coupled viscoelastic behavior, the higher loading rate also leads to more rate-dependent damage behavior at the end of the displacement loading. Park, et al. (1996) conducted the uniaxial tension experiment with the asphalt concrete sample at different strain rates, and the test data about the damage evolution with strain also shows such a damage increase with loading rate. Figure 6.8(b) shows the

simulation results under cyclic linear displacement loading (± 5mm) but with different loading rates 1, 0.5 and 0.33 mm/s. Results indicate that the higher loading rate also leads to a stiffer specimen under cyclic loading. The Mullins effect is also demonstrated in these simulation results under constant loading rate.

Simulations were also conducted with different material properties for a loading history with three loading rate increments as shown in Fig. 6.9. A threshold strain rate was chosen as $\dot{e}_C = 0.001$. Figure 6.9(a) shows the compression displacement input indicating the three loading rate increments. Figure 6.9(b) shows the simulation results with four types of mastic material properties: linear viscoelastic, rate-independent damage with a = 0, and rate-dependent damage with a = 0.1 and 0.3. Comparison between linear and rate-independent damage behavior shows that the rate-independent damage again increases with the loading displacement. Comparisons between two rate-dependent damage cases (a = 0.1 and 0.3) and rate-independent damage (a = 0) behavior, indicate additional rate-dependent damage increases with the loading rate. Also more rate-dependent damage is generated with a larger a parameter.

6.4.3 Qualitative Comparison of Uniaxial Tensile Simulation with Test Data

A computation sample for uniaxial tensile simulation is generated as shown in Fig. 6.10. This model has 142 particles (in three particle size group of 7, 9, 11 mm), 447 effective mastic zones and zero porosity. This rectangular sample has the geometry of width 110 mm, height 102 mm and thickness 25 mm, and includes 1788 deforming mastic elements and 1170 rigid aggregate elements. These simulation used 3-parameter viscoelastic constitutive properties for the mastic elements, including relaxation modulus $E_\infty = 1.586$ MPa and one Maxwell elements E_1= 145MPa and r_1= 0.5 s. These constitutive properties are from characterization test data by Lee and Kim (1998). And the Possion's Ratio was chosen as 0.3.

Uniaxial tension simulations were conducted under the constant-strain-rate monotonic displacement loading and with varying strain rates. For these simulations, the damage parameters are same as loading rate study. Figure 6.11 shows the comparison of uniaxial tensile simulation and test data with different strain rates. These experimental data are obtained from the constant-strain-rate uniaxial extension tests by Lee and Kim (1998). In the simulations, axial strain was calculated by dividing the elongation by the initial height of the undeformed sample, and axial stress was obtained by dividing the summed reaction particle force on the top layer by the sample initial cross-section area. Comparison was made at different strain rate of 0.0032, 0.0016 and

0.0004. By choosing these damage parameters, the simulation results on this idealized microstructure sample can qualitatively match these experimental data. Thus this study shows damage-coupled viscoelastic model can predict this type of asphalt behavior with different loading strain rates.

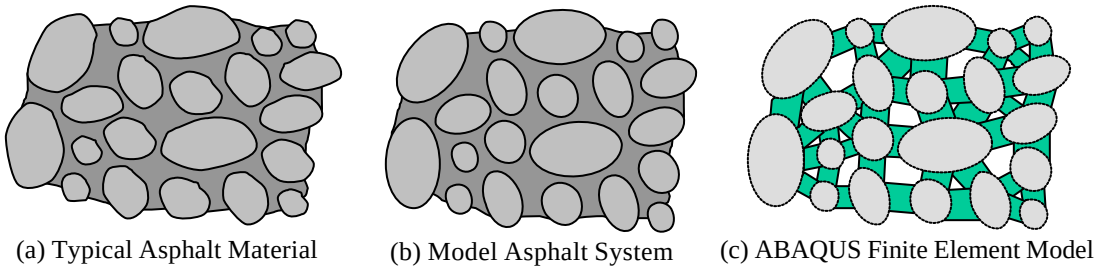

(a) Typical Asphalt Material (b) Model Asphalt System (c) ABAQUS Finite Element Model

Fig. 6.1 Asphalt modeling concept

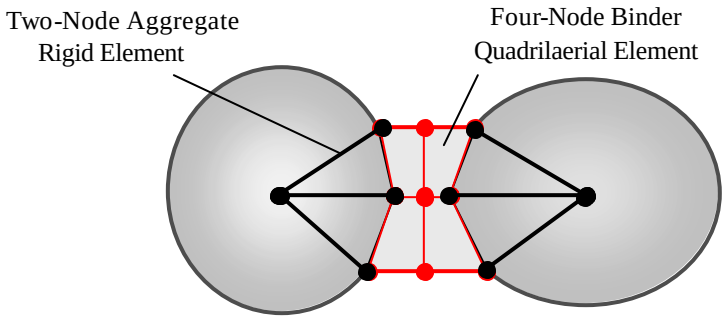

Fig. 6.2 ABAQUS modeling scheme for a typical particle pair

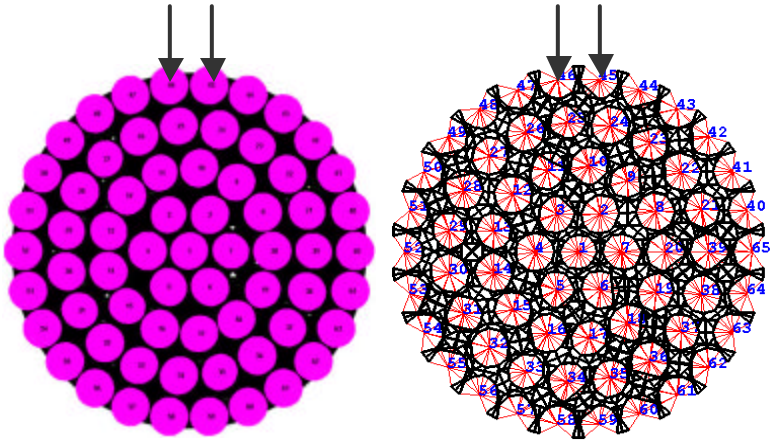

Numerical Sample Mesh Sample

Fig. 6.3 Indirect tension numerical sample

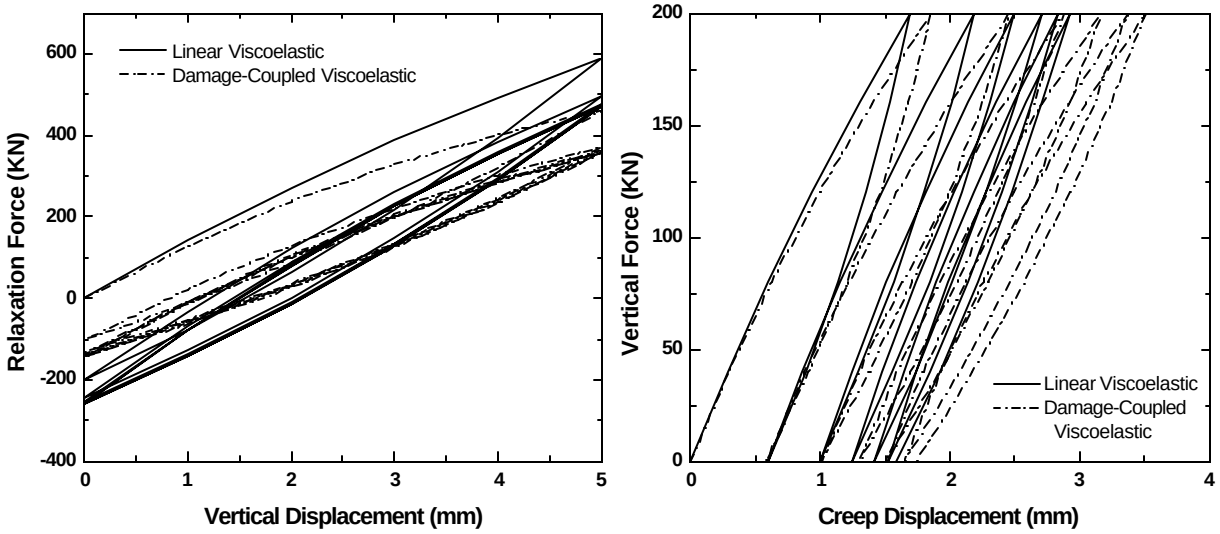

(a) Displacement control (b) Force control

Fig. 6.4 Unreversed saw-toothed loading

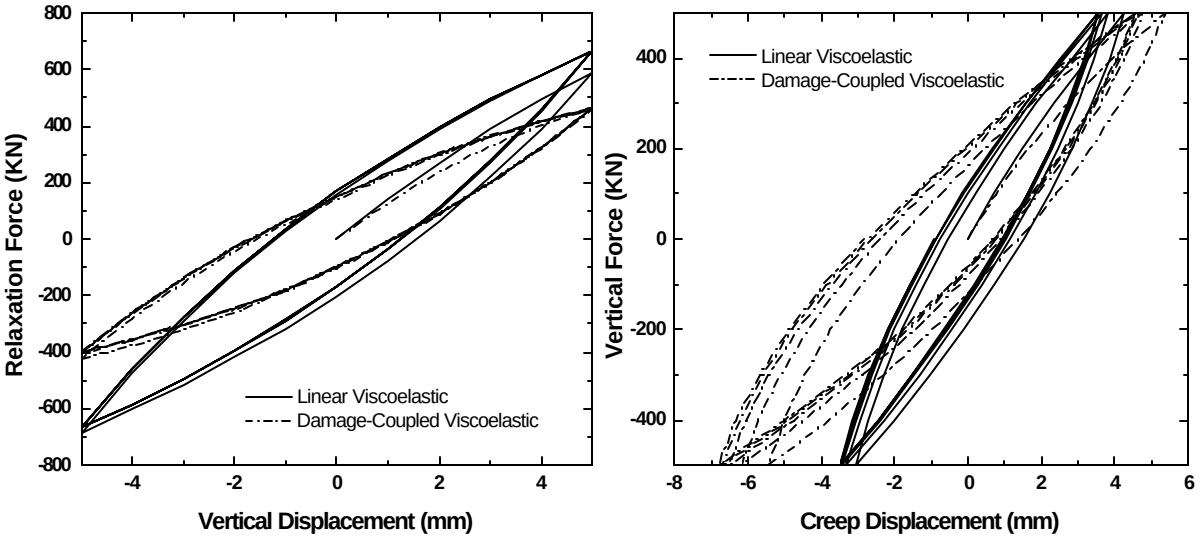

(a) Displacement control (b) Force control

Fig. 6.5 Reversed saw-toothed loading

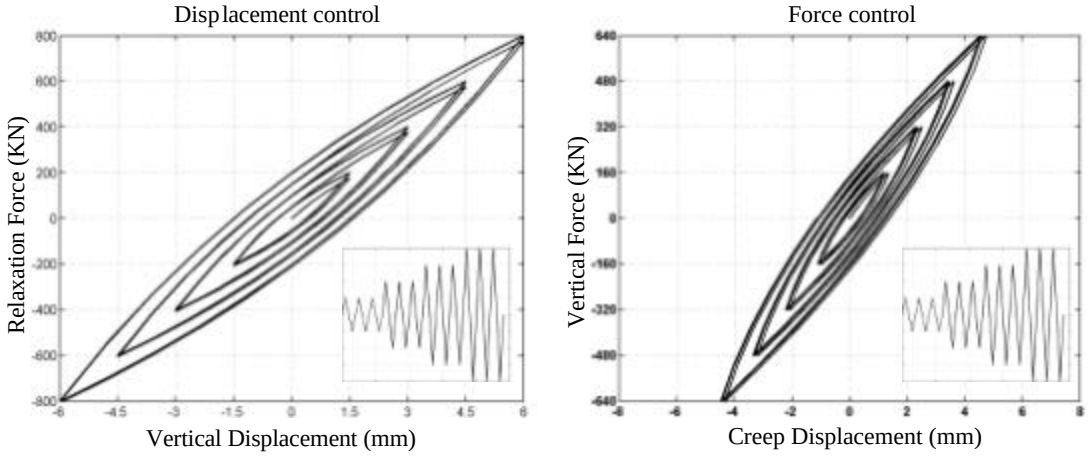

(a) Linear viscoelastic response

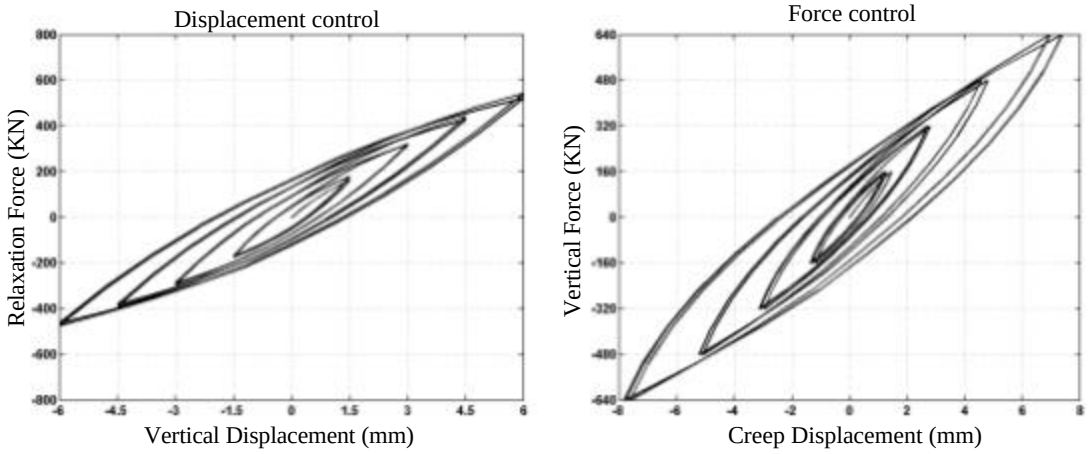

(b) Damage-coupled viscoelastic response

Fig. 6.6 Incrementally increasing reversed cyclic loading

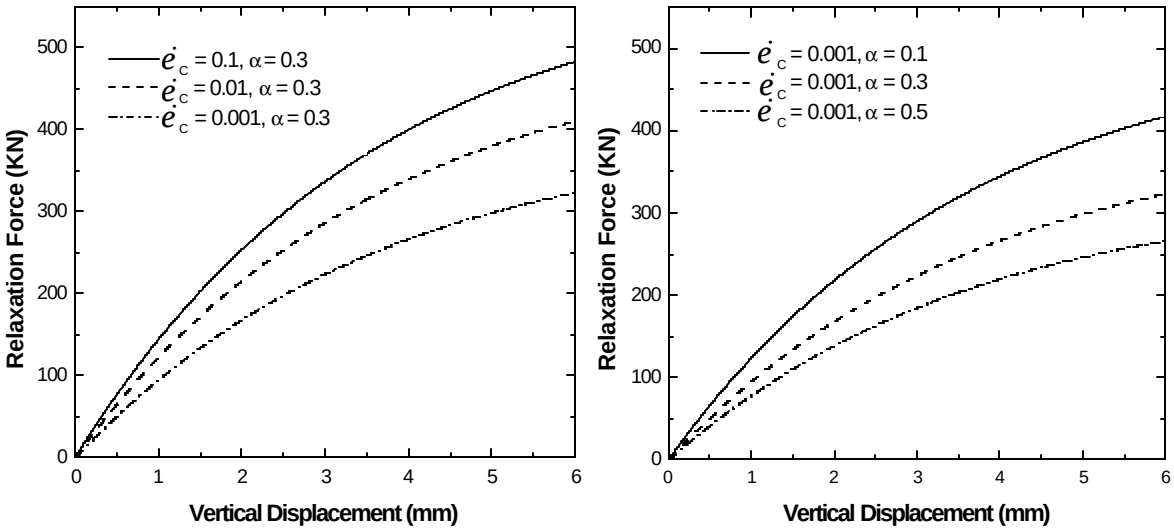

(a) Simulation with different $\dot{e}_C$ (b) Simulation with different a

Fig. 6.7 Parameter study of rate-dependent damage variable h_2

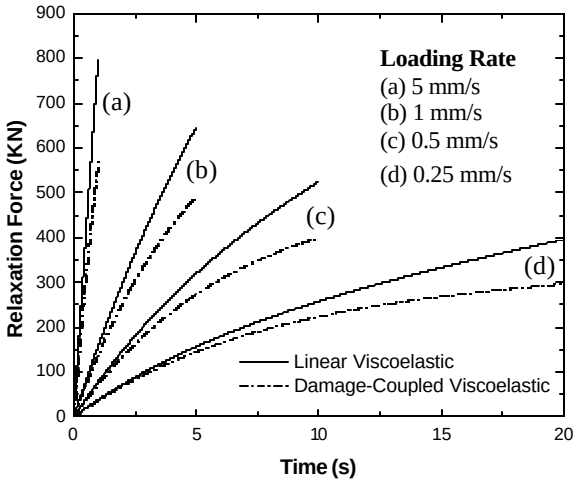

(a) Simulations under monotonic linear loading

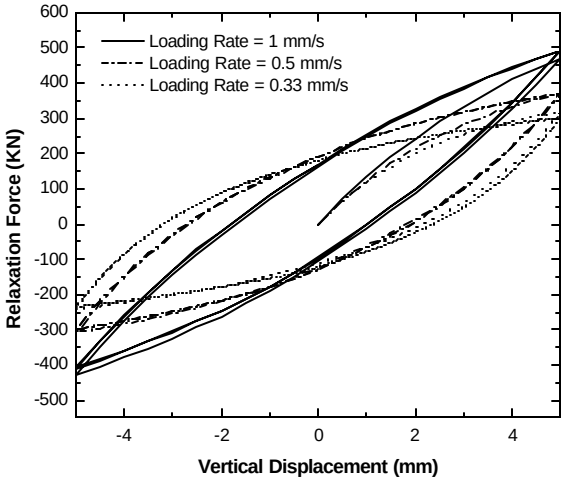

(b) Simulations under cyclic linear loading

Fig. 6.8 Loading rate effect on the asphalt viscoelastic damage behavior

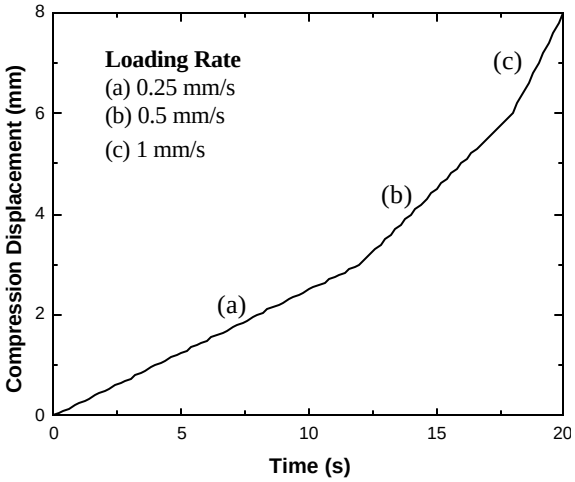

(a) Compression displacement

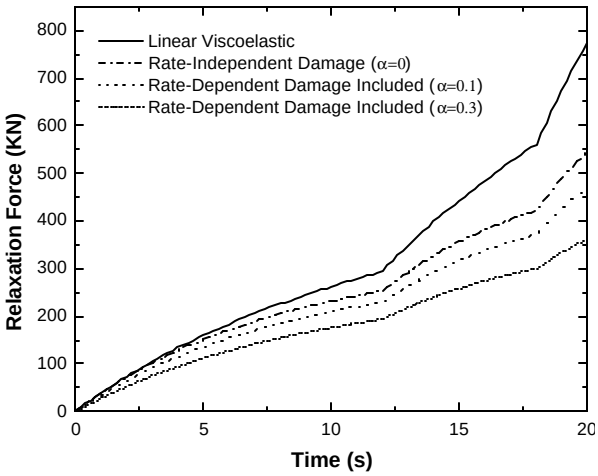

(b) Simulations with different material properties

Fig. 6.9 Simulations under three loading rate increments

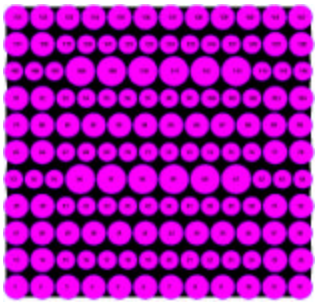

Fig. 6.10 Uniaxial tension numerical model

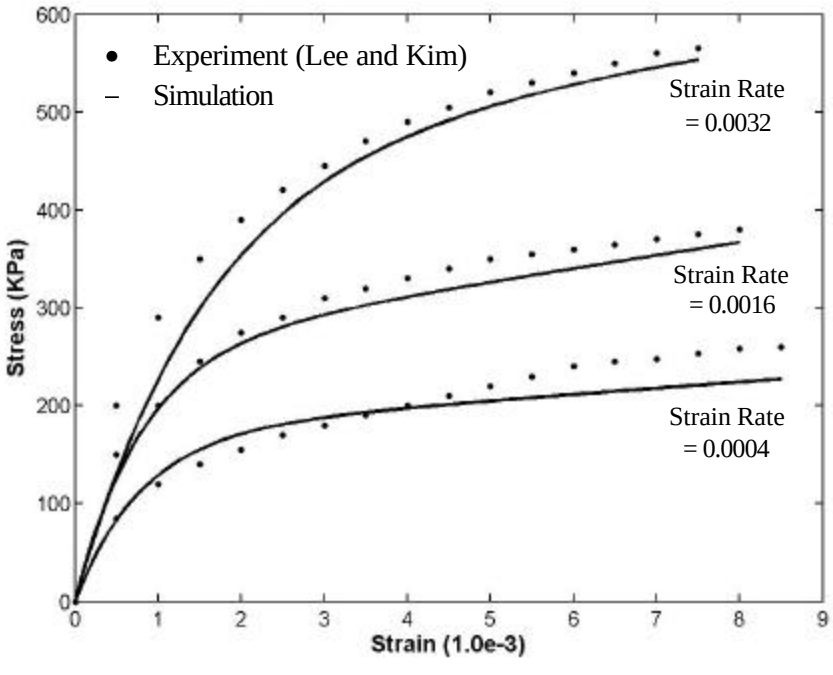

Fig. 6.11 Uniaxial stress-strain behavior at different strain rates

7. SUMMARY AND CONCLUSIONS

The experimental program investigated quasi-static and rate dependent properties of asphalt samples containing 30% RAP. The testing program was conducted on standard compression and indirection tension samples, and three-point bend fracture specimens were also included. Quasi-static loading was conducted using an Instron testing machine, while dynamic loading was done in two different Hopkinson Pressure Bar apparatus.

Results of compression and indirect tension testing indicated that the material had significant rate sensitivity. The average dynamic compressive strength was about five (5) times the corresponding static value, while tensile strength also showed an increase by a factor 1.5. The fracture behavior was characterized using the stress intensity factor (SIF), and it was found that the dynamic SIF was 15 times greater than the static value. Thus the material offers higher resistance to all modes of deformation and failure under dynamic conditions. Table 7.1 summarizes the findings of the experimental program.

Table 7.1 Comparison of mechanical properties characterized in the study

Property	***Quasi-Static Loading***	***Dynamic Loading***	***Dynamic/Static Ratio***
Uniaxial Compressive Strength (MPa)	3.55	15-25	5
Indirect Tension Strength (MPa)	1.32	1.53	1.5
Fracture Toughness - Critical Stress Intensity Factor (MPa$\sqrt{m}$)	0.11	2.00	18

Post mortem analysis of the damage and fractured specimens revealed substantial differences in the failure processes between static and dynamic loadings. Quasi-static loadings generally produced failure in the binder material, and thus binder strength and adhesion with the aggregates provide the overall strength. However, for the dynamic loading cases trans-aggregate failure (fracture of aggregates) commonly occurred. We would thus conclude that the strength and deformation response of asphalt materials under dynamic loading conditions would be related to both trans-aggregate fracture and binder material stiffening due to rate dependent effects.

The numerical study developed a micromechanical constitutive model to simulate the rate dependent two-dimensional viscoelastic damage behavior of asphalt materials. The aggregate-binder microstructure was simulated by using continuum elements for the asphalt mastic and rigid body elements for each aggregate. Rate-independent failure and rate-dependent damage mechanisms were developed and combined within Schapery nonlinear viscoelasticity theory. A finite element incremental algorithm with recursive relationships for the 3D viscoelastic damage behavior was developed. The numerical implementation of this method was done using the ABAQUS user material subroutine for the asphalt mastic to predict global viscoelastic damage behavior of asphalt materials.

The cyclic loading response of linear and rate-independent damage viscoelastic asphalt materials were compared for both displacement- and force-controlled boundary conditions. These cyclic loading responses show rate-independent damage increases with the maximum deformation and also demonstrate the Mullins effect. The study of loading rate effects showed that higher loading rate leads to a stiffer asphalt sample response and also generates more rate-dependent damage behavior. By using the unified damage model, this study also compared the viscoelastic response of linear, rate-independent damage, and rate-dependent damage material properties under different loading rate and amplitude.

In general model results gave simulations that were in qualitative agreement with observed and expected behavior of asphalt materials. The preliminary model verification study shows viscoelastic damage simulation on the idealized microstructure can match uniaxial tensile test data. More detailed experimental test data is needed to further verify the quantitative results of this modeling effort.

8. ACKNOWLEDGEMENTS

The authors would like to acknowledge supported from the Transportation Center at the University of Rhode Island under Grant 536186. Additional support was also provided from Cardi Construction Corporation.

9. PRESENTATIONS AND PUBLICATIONS

Presentations and publications of the work during this project period include:

"Microstructural Simulation of Asphalt Samples Using a Finite Element Network Model", Q. Dai and M. Sadd, 16th ASCE Engineering Mechanics Conf., University of Washington, Seattle, WA, June 2003.

"Effect Of Loading Rate On The Splitting Strength Of Recycled Asphalt Concrete", SEM Student Conference, Worcester Polytechnic Institute, Worcester, MA, 2003

"High Strain Rate Characterization of RAP Mix", SEM Graduate Students Symposium on Mechanics and Packaging, Worcester Polytechnic Institute, Worcester, MA, 2004 (Best Paper Award)

"On the Use of Doublet Mechanics for Microstructural Modeling of Cemented Particulate Materials", M. Sadd and Q. Dai, 17th ASCE Engineering Mechanics Conf., University of Delaware, Newark, DE, June 2004.

"Micromechanical Modeling of Damage-Coupled Viscoelastic Behavior of Asphalt Materials", Q. Dai and M. Sadd, 17th ASCE Engineering Mechanics Conf., University of Delaware, Newark, DE, June 2004.

"A Comparison of Micromechanical Modeling of Asphalt Materials Using Finite Elements and Doublet Mechanics", M. Sadd and Q. Dai, to appear in *Mechanics of Materials*.

"Parametric Model Study of Microstructural Effects On Damage Behavior of Asphalt Samples", Q. Dai and M. Sadd, to appear in *International Journal of Pavement Engineering*.

"A Micromechanical Constitutive Model for Damage-Coupled Viscoelastic Behavior of Asphalt Materials" Q. Dai and M. Sadd, to appear in *Journal of Applied Mechanics*.

10. REFERENCES

ASTM D 5045-93, 1993, *"Plane-strain fracture toughness and strain energy release rate of plastic materials"*, ASTM Publication.

Anderson, T.L., 1995, *"Fracture mechanics: fundamentals and applications"*, Second Edition CRC Press, USA.

Baker, W.E., and Yew, C.H., 1966, *"Strain rate effects in the propogation of torsional plastic waves "*, Journal of Applied Mechanics, Transactions ASME, Vol. 33, pp. 917.

Bahia, H., Zhai, H., Bonnetti, K., and Kose, S., 1999, *"Nonlinear Viscoelastic and Fatigue Properties of Asphalt Binders*", Journal of Association of Asphalt Paving Technologists, Vol. 68, pp. 1-34.

Canga, M. E., Becker, E. B., and Özüpek, S., 2001, *"Constitutive Modeling of Viscoelastic Materials with Damage – Computation Aspects*", Computer Methods in Applied Mechanics and Engineering, Vol. 190, pp. 2207-2226.

Chaboche, J.L., 1988, *"Continuum Damage mechanics, Parts I and II*", ASME Journal of Applied Mechanics., Vol. 55, pp. 59-72.

Chen, W., Zhang, B.Z., and Forrestal, M.J., 1999,*"A split Hopkinson bar technique for low-impedance materials"*, Experimental Mechanics, Vol. 39(2), pp. 81-85.

Chiddister, J.L., and Malvern, L.E., 1963, *"Compression impact testing of aluminum at elevated temperatures*", Experimental Mechanics, Vol. 3, pp. 81-90.

Dai, Q. L. and Sadd, M. H., 2004, "*A Micromechanical Constitutive Model for Damage-Coupled Viscoelastic of Asphalt Materials*", Submitted to ASME Journal of Applied Mechanics.

Davies, R. M., 1948, "*A critical study of the Hopkinson Pressure Bar*", Philosophical Transactions of the Royal Society of London, Series B, Vol. 240, pp. 375-457.

Davies, E.D.H., and Hunter, S.C., 1963, *"The dynamic compression testing of solids by the method of the split Hopkinson pressure bar"*, Journal of the Mechanics and Physics of Solids, Vol. 11(3), pp. 155-179.

Evora, V.M.F, and Shukla, A., 2003, *"Fabrication, characterization, and dynamic behavior of polyester/TiO_2 nanocomposites"*, Materials Science and Engineering A, Vol. 361(1-2), pp. 358-366.

Evora, V.M.F, 2004, *"Fabrication and dynamic mechanical behavior of nano composites"*, Doctoral Dissertation, University of Rhode Island, USA.

Gibson, N. H., Schwartz, C. W., Schapery, R. A. and Witczak, M. W., 2003, "*Viscoelastic, Viscoplastic, and Damage Modeling of Asphalt Concrete in Unconfined Compression*", Proceedings of 82nd Transportation Research Board Meeting, Washington, D.C.

Gomez, J.T., Shukla, A., and Sharma, A., 2001, *"Static and dynamic behavior of concrete and granite in tension with damage"*, Journal of Theoretical and Applied Fracture Mechanics, Vol. 36, pp. 37-49.

Gomez, J.T., Shukla, A., and Sharma, A., 2002, *"Photoelastic evaluation of stress field and fracture during dynamic splitting experiments"*, Journal of testing and Evaluation, JTEVA, Vol. 30(3), pp. 186-196.

Guddati, M.N., Feng, Z., and Kim, Y.R., 2002, "*Towards a Micromechanics-Based Procedure to Characterize Fatigue Performance of Asphalt Concrete*", Proceedings of 81st Transportation Research Board Meeting, Washington, D.C.

Haj-Ali, R. M., and Muliana, A. H., 2003, "*A Micromechanical Constitutive Framework for the Nonlinear Viscoelastic Behavior of Pultruded Composite Materials*", International Journal of Solids and Structures, Vol. 40, pp. 1037-1057.

Harding, J., Wood, E.D., and Campbell, J.D., 1960, Journal of Mechanical Engineering, Vol. 2, pp. 88-96.

Hesp, S.A.M., Hoare, T.R., and Roy, S.D., 2002, *"Low- temperature fracture in reactive-ethylene-terpolymer-modified asphalt binders"*, The International Journal of Pavement Engineering, Vol. 3(3), pp. 153-159.

Hopkinson, B., 1914, " *A method of measuring the pressure produced in the detonation of explosives or by the impact of bullets*", Philosophical Transactions of the Royal Society of London, Series A, Vol. 213, pp. 437-456.

Kachanov, M., 1987, *"On Modeling of Anisotropic Damage in Elastic-Brittle Materials-A Brief Review*", *Damage Mechanics in Composite,* Wang, A.S.D., and Haritos, G.K., ed., ASME, pp. 99-105.

Kaliske, M., Nasdala, L., and Rothert, H., 2001, *"On Damage Modeling for Elastic and Viscoelastic Materials at Large Strain*", Computers & Structures, Vol. 79, pp. 2133-2141.

Kim, K.W., and El Hussein, M., 1997, *"Variation of fracture toughness of asphalt concrete under low temperatures"*, Construction and Building Materials, Vol. 11(7-8), pp. 403-411.

Kim, K.W., Young S.D., and Sungbin, L., 1999, *"Mode I reflection cracking resistance of strengthened asphalt concretes"*, Construction and Building Materials, Vol. 13(5), pp. 243-251.

Kim, K.W., Kweon, S.J., Young S.D., and Park, T.S., 2003, *"Fracture toughness of polymer modified asphalt concrete at low temperature"*, Canadian Journal of Civil Engineering, Vol. 8, pp. 406-413.

Kolsky, H., 1949, *"An investigation of the mechanical properties of materials at very high strain rates*", Philosophical Transactions of the Royal Society of London, Series B, Vol. 62, pp.676-700.

Kumar, R. S., and Talreja, R., 2001, *"A Continuum Damage Model for Linear Viscoelastic Composite Materials*", Mechanics of Materials, Vol. 35, pp. 463-480.

Lee, H.J., Kim, Y.R., 1998, *"Viscoelastic Constitutive Model for Asphalt Concrete Under Cyclic Loading*", Journal of Engineering Mechanics ASCE, Vol. 124(1), pp. 32-40.

Lindholm, U.S., 1964, *"Some experiments with the split hopkinson pressure bar"*, Journal of the Mechanics and Physics of Solids, Vol. 12(5), pp. 317-335

Malvern, L.E., and Ross, C.A., 1985, *"Dynamic response of concrete structures", 1982-85, "AFOSR Contract No. FR9620-83-K007*", US Air Force office of scientific research, Aerospace Directorate, Bolling Air Force Base, D.C.

Marigo, J. J., 1985, *"Modelling of Brittle and Fatigue Damage for Elastic Material by Growth of Microvoids*", Engineering Fracture Mechanics, Vol. 21, pp. 861-874.

Martins, C.F., and Prakash, V., 2002, *"Dynamic fracture of linear medium density polytethylene"***,** Proceedings of the TMS Fall Meeting, pp. 105-122.

Mobasher, B., 1997, *"Evaluation of crack propogation properties of asphalt mixtures"*, Journal of Transportation Engineering, pp. 405-413.

Mullins, L., 1969, *"Softening of Rubber by Deformation*", Rubber Chemical Technology, Vol. 42, pp. 339-362.

Park, S.M., Kim, Y. R., and Schapery, R.A., 1996, "*A Viscoelastic Continuum Damage Model and Its Application to Uniaxial Behavior of Asphalt Concrete*", Mechanics of Materials, Vol. 24, pp. 241-255.

Park, S.M., and Schapery, R.A., 1996, "*A Viscoelastic Constitutive Model for Particulate Composites with Growing Damage*", International Journal of Solids and Structures, Vol. 34(8), pp. 931-947.

Sadd, M.H., "*Wave Motion and Vibration of Continuous Media*", Class Notes (2000).

Sadd, M.H., Dai, Q.L., Parameswaran, V. and Shukla, A., 2004a, "*Microstructural Simulation of Asphalt Materials: Modeling and Experimental Studies*", Journal of Materials in Civil Engineering, ASCE, Vol. 16(2), pp. 107-115.

Sadd, M.H., Dai, Q.L., Parameswaran, V., and Shukla, A., 2004b, "*Simulation of Asphalt Materials Using a Finite Element Micromechanical Model and Damage Mechanics*", Journal of Transportation Research Board, Vol. 1832, pp. 86-94.

Schapery, R. A., 1969, "*On the Characterization of Nonlinear Viscoelastic Materials*", Polymer Engineering and Science, Vol. 9(4), pp. 295-310.

Schapery, R.A., 1984, "*Corresponding Principles and a Generalized J Integral for Large Deformation and Fracture Analysis of Viscoelastic Media*", International Journal of Fracture, Vol. **25**, pp. 195-223.

Schapery, R.A., 1991, "*Analysis of Damage Growth in Particulate Composite Using a Work Potential*", Composites. Part B, Engineering, Vol. 1(3), pp. 167-182.

Schapery, R.A., 1999, "*Nonlinear Viscoelastic and Viscoplastic Constitutive Equations with Growing Damage*", International Journal of Fracture, Vol. 97, pp. 33-66.

Sepehr, K., Harvey, O.J., Yue, Z.Q., and El Husswin, H.M., 1994, "*Finite Element Modeling of Asphalt Concrete Microstructure*", Proceedings of 3rd International Conference of Computer-Aided Assessment and Control Localized Damage, Udine, Italy.

Simo, J.C., 1987, "*On a Fully Three-Dimensional Finite-Strain Viscoelastic Damage Model: Formulation and Computational Aspects*", Computer Methods in Applied Mechanics and Engineering, Vol. 60, pp. 153-173.

Simo, J. C., and Ju, J. M., 1987, "*Strain- and Stress-Based Continuum Damage Models I. Formulation*", International Journal of Solids and Structures, Vol. 23(7), pp. 821-840.

Soares, J.B., Colares de Freitas, F.A. and Allen, D.H., 2003, "*Crack Modeling of Asphaltic Mixtures Considering Heterogeneity of the Material*", Proceedings of 82nd Transportation Research Board Meeting, Washington, D.C.

Starodubsky, S., Blechman, I., and Livneh, M., 1994, "*Stress-strain relationship for asphalt concrete in compression*", Journal of Materials and Structures, Vol.27, pp. 474-482.

Venkatram, S., 1997, *"Fracture toughness and dynamic constitutive characterization of recycled asphalt pavement binder"*, Masters thesis, University of Rhode Island, USA.

Wu, R. Z. and Harvey, J. T., 2003, "*Modeling of Cracking in Aspect Concrete with Continuum Damage Mechanics*", Proceedings of 12th ASCE Engineering Mechanics Conference, Seattle, WA.

Zotch, M. A., and Groves, S. E., 1997, "*A Three-Dimensional Finite Element Formulation for Thermoviscoelastic Orthotropic Media*", International Journal of Numerical Methods in Engineering, Vol. 40, pp. 2267-2288.